POSTER SESSION

PARTITIONING AND ACCELERATOR DRIVEN TRANSMUTATION

EXTRACTION OF AM(III) AND EU(III) BY 2,6-DI(5,6-DIALKYL-1,2,4-TRIAZIN-3-YL)PYRIDINES

Zdenek Kolarik and Udo Müllich
Forschungszentrum Karlsruhe,
Institut für Nukleare Entsorgungstechnik,
P.O. Box 3640, 76021 Karlsruhe,
Germany

Abstract

It had previously been shown that 2,6-di(5,6-dialkyl-1,2,4-triazin-3-yl)pyridines extract Am(III) selectively over Eu(III), giving a separation factor of 100-120. In this work a more detailed study of the distribution equilibria was made. If not given otherwise, 2,6-di(5,6-dipropyl-1,2,4-triazin-3-yl)pyridine (= B) was taken as a representative of the title extractant class and a mixture of branched alkanes (TPH) modified with 2-ethyl-1-hexanol was taken as a diluent. Since Am(III) and Eu(III) (=M) are extracted as complexes of the type $M(NO_3)_3 3B$, their distribution ratios increase strongly with the activity of nitrate ions in the aqueous phase and the concentration of the extractant in the organic phase. The distribution ratios of the metals are suppressed in the presence of macro amounts of Eu(III), due to lowering the free extractant concentration as the solvent loading is not negligible, but the Am(III)/Eu(III) separation factor remains unchanged. The extraction of Am(III) and Eu(III) is little changed if 1-octanol is taken as a TPH modifier instead of 2-ethyl-1-hexanol, and the highest distribution ratios are attained at 10 - 20 vol% alcohol. The optimum concentration of the alcohol is 20 vol%, giving appropriate solubilization of the extractant in the mixed diluent. Higher distribution ratios are obtained in the presence of 1-butanol which, however, solubilizes the extractant less effectively than the octanols. Both the extraction efficiency and the Am(III)/Eu(III) separation factor decrease in the following order of diluents (each modified by 20 vol% 2-ethyl-1-hexanol): TPH > cyclohexane >2-methyl-4-pentanone > 2-ethylhexyl acetate > chlorobenzene > benzene > xylene.

NEW MOLECULES FOR AN(III)/LN(III) SEPARATION BY LIQUID LIQUID EXTRACTION

P.Y. Cordier, C. Hill, C. Madic
CEA-Valrhô DCC/DRRV/SEMP
Marcoule, BP 171
30207 Bagnols-sur-Cèze
France

Z. Kolarik
Forschungszentrum Karlsruhe (FZK), INE
P.O. Box 3640, 76021 Karlsruhe
Germany

Abstract

The separation of trivalent actinides, americium and curium, from actinides and lanthanides mixtures is an important step in an advanced partitioning process for wastes issued from the reprocessing of spent nuclear fuel. Our goal is to allow the An(III) selective extraction from concentrated nitric acid solutions (up to 1 mol/l), using if possible potentially incinerable molecules, containing only C, H, O and N.

We present here a new family of An(III) selective extractants, the 2,6-bis-(5,6-di-n-alkyl-1,2,4-triazin-3-yl)-pyridine named thereafter BTP (Bis Triazin Pyridin). These molecules were designed by Z. KOLARIK at the KFZ, member of the NEWPART contract, and seem able to fulfil this goal.

These molecules exhibit very strong extracting properties, allowing Am(III) to be extracted from nitric solutions ($D_{Am(III)} > 2$ for $[HNO_3] = 1$ mol/L), with a very good separation factor over Eu(III) ($FS_{Am/Eu} > 100$).

The first studies conducted on this family of molecules show that:

- The kinetics of the extraction is rather slow (time to reach equilibrium is around 1 hour, in batch test tube conditions), and depends on the nature of the alkyl substituents (equilibrium is faster for *n*-Propyl BTP than for *n*-Butyl-BTP). The kinetics do not seem to be affected by the concentration of the extractant, the concentration of nitric acid or nitrate ions in a wide range.

- The extraction and separation performances are influenced by the nature of the diluent. A mixture of non polar diluent (hydrogenated tetrapropene) and polar one (*n*-octanol), in a volume ratio (80/20) is needed to solubilise the BTP, and ensure the best performances. Dissociating diluent (Nitrophenyl-Octylether, Nitrobenzene) gives good extraction, thus suggesting a solvatation extraction mechanism, but lower separation factor. Aromatic diluent such as Tertiary-butyl-benzene gives poor extraction and separation performances, but a fast kinetic.
- The BTP appears to have a very low basicity, compare to other nitrogen bearing ligands. A relative scale of pKa was established, in methanol/water media, and shows that the pKa of BTP was lower from 1 to 2 units than the ones of Terpyridine or tripyridiltriazine (TPTZ). This property can explain the extraction performances at high nitric acid concentration, the competition H^+ / M(III) complexation shifting towards the M(III) side.

These results show that it should now be possible to design a process for the selective extraction of An(III) over Ln(III) from high-level liquid wastes, using only disposable molecules and diluent. Such a process will be tested in hot conditions at the Transuranium Elements Institute (TUI, NEWPART member), on a PUREX / DIAMEX raffinate very soon.

SYNERGISTIC SYSTEMS USING POLYPYRIDINES AND CARBOXYLIC ACIDS FOR THE AN(III) / LN(III) SEPARATION

P.Y. Cordier, C. Madic
CEA-Valrhô DCC/DRDD/SEMP,
Marcoule
BP 171
30207 Bagnols-sur-Cèze
France

J.O. Liljenzin
Department of Chemistry
University of Reading
Box 224, Whiteknights
Berkshire RG6 2AD
UK

P. B. Iveson, M. J. Hudson
Department of Nuclear Chemistry
Chalmers University of Technology
41296 Göteborg
Sweden

Abstract

The separation of trivalent actinides, americium and curium, from actinides and lanthanides mixtures is an important step in an advanced partitioning process for wastes issued from the reprocessing of spent nuclear fuel. To achieve this separation, synergistic systems were tested, with 2-bromodecanoic as a cationic exchanger and different nitrogen bearing ligands.

The groups of ligands tested are:

- 2,2':6',2"-terpyridine (Tpy) and alkylated derivatives.
- 2,4,6-tri-(pyrid-2-yl)-1,3,5-triazine (TPTZ) and alkylated derivatives.
- Alkylated Tetra and Penta pyridine.
- 2-amino-4,6-di-(pyrid-4-yl)-1,3,5 triazine (ADPTZ) and alkylated derivatives.

All these ligands were tested in synergistic systems with 2-bromo-decanoic acid. The main results we can draw about these experiments are:

- The basicity of the molecule is a key point for the extraction performances at low pH of the aqueous phase. Only molecules with a low pKa (TPTZ) can extract M(III) from such a media.
- The number of nitrogen directly in contact with the metal has a positive effect on the separation factor $SF_{Am/Eu}$, and sometimes on the distribution ratio $D_{M(III)}$. Tetra and Penta Pyridine offers $SF_{Am/Eu}$ around 20, while Tpy is around 10.
- The electronic configuration of the binding site appears to be the most important factor for the extraction. The change in position and number of nitrogens in the heteroaromatic cycle leads to very important modifications of the properties ($D_{M(III)}$ and $SF_{Am/Eu}$).
- The lipophilic character of the molecule has a secondary effect on the extraction, less important than the electronic property of the binding site. In some case (TPTZ) the alkylation of the basic molecules leads to en enhancement in the extraction properties. In some other case (Tpy), this leads to a decrease of the M(III) distribution ratio. This phenomenon can be due to steric hindrance, or to a small modification of the electronic configuration of the binding site.

The results gathered by this comparative study lead to a better knowledge of the properties required to design a selective extracting system from high acidity aqueous phase: the ligand should have a low basicity, a tri or quaterdendate binding site, and as many nitrogen atoms as possible inside the aromatic rings.

SYNERGISTIC "An(III)/Ln(III)" SEPARATION WITH DITHIOPHOSPHINIC EXTRACTANTS AND RELATED MLCT PHENOMENA

C. Hill, C. Madic
CEA-Valrhô DCC/DRRV/SEMP
Marcoule
BP 171
30207 Bagnols-sur-Cèze
France

G. Modolo
Forschungszentrum Jülich
Institut für Sicherheitsforschung und
Reaktortechnik ISR-3
52425 Jülich
Germany

Abstract

The study of the extraction properties and the selectivity of synergistic mixtures, based on dithiophosphinic acids and oxygen atoms bearing extracting agents was conducted at Marcoule Centre. Visible spectroscopy was applied to point out the occurrence of Ligand to Metal Charge Transfer (LMCT) phenomena when using these organic solutions to extract europium (III).

In the case of "purified Cyanex 301 acid/TBP" mixtures, the separation factor between americium and europium, was maximum for $10\%_{molar}$ TBP ($S.F._{Am/Eu} > 5000$, with $D_{Am} \sim 200$). This particular molar ratio was chosen for the comparison between various synergistic mixtures, based on purified Cyanex 301 acid and oxygen atoms bearing extracting agents, such as phosphates, phosphine oxides, monoamides and diamides. The extraction and separation properties were compared at pH ~ 3. Synergistic as well as antagonistic effects were observed, depending on the nature of the solvating agent. Three different behaviours could be distinguished :

Compounds such as phosphine oxides promoted ^{241}Am and ^{152}Eu extraction as compared to purified Cyanex 301 acid alone, but with a far lower $S.F._{Am/Eu}$.

Compounds such as sterically hindered phosphates favoured Am/Eu separation but showed poorer extracting properties than purified Cyanex 301 acid alone.

Compounds such as TBP, DOTA (monoamide) or DPSO (sulphur oxide) promoted both the extraction of ^{241}Am and ^{152}Eu and their separation. A $S.F._{Am/Eu}$ as high as 15000 was observed for trace level ^{241}Am and ^{152}Eu in the case of DOTA, while Cyanex 301 acid alone showed a $S.F._{Am/Eu}$ of ~ 5000, at pH ~ 3.

Purified Cyanex 301 acid was uncoloured in dodecane, whereas it became yellowish when loaded with europium(III) : the band of LMCT appeared at 434 nm. Small additions of TBP not only intensified the band of charge transfer of europium(III), but also induced a "blue-shift". The colour of the organic solutions turned to deep orange as the concentration of TBP increased, and so up to $10\%_{molar}$ TBP in the synergistic mixture.

Visible spectroscopy was also applied to all previously described synergistic mixtures, composed of purified Cyanex 301 acid on the one hand, and oxygen atoms bearing solvating agents on the other hand. It was rather difficult to explain the differences observed in the behaviour of monodendate ligands (phosphates or monoamides) and bidendate ligands (CMPO or diamide) or between strong and medium electron donating ligands (phosphine oxides *vs* TBP, diamide *vs* monoamide). However, it seemed that whenever a high $S.F._{Am/Eu}$ was obtained for trace level ^{241}Am and ^{152}Eu, a strong LMCT phenomenon was also observed.

Three different bis(*R*-phenyl)dithiophosphinic acids (*R* = -H, -Cl and -F) were also tested in synergistic mixtures with TOPO and their extracting properties checked at medium acidity ($[HNO_3] \sim 0.5$ mol/L). In this case, only weak Eu(III) LMCT phenomena were observed ; the loaded organic solutions were bright yellow and the maximum absorption bands could not be clearly pointed out.

MOLECULAR DYNAMICS SIMULATIONS OF POLYPYRIDINES WITH LANTHANIDES

P. Guilbaud, J. P. Dognon
CEA-Valrho, DCC/DRRV/SEMP
Bât. 166
BP 171
30207 Bagnols/Ceze
France

Polypyridines have been studied in our laboratories as selective extractants of actinides(III) versus lanthanides(III) using a synergistic mixture with aliphatic carboxylic acids. Our aim in this study was, using theoretical chemistry, to better understand the actinide and lanthanide trivalent cations complexation with polypyridines. We first decided : (i) to focus on small polypyridine units studying the terpyridine ligand (ii) to select three lanthanide ions (La^{3+}, Eu^{3+} and Lu^{3+}). Molecular dynamics (MD) simulations have been performed for timescales between 100 and 500 ps using the AMBER software. These calculations are related to : (i) the gas phase and (ii) water solutions, with an explicit representation of the solvent.

The free terpyridine ligands have been simulated in the water phase in order to investigate the influence of the water solvation on their conformation. The interaction between water molecules and the terpyridines stabilises the 111 conformers over the two others conformers. Using the Gibbs free energy perturbation theory, one is able to calculate the $\Delta\Delta G$ between two conformers. In the water phase, this calculation, that takes into account the entropy differences, reveal no energy differences between the three conformers. The water stabilises the 111 conformer over the two others, but there is no real preorganisation of the ligand. The (Ln^{3+}/terpyridine) complexes have been simulated in the gas phase and in water solution with different counter ions. This study demonstrates that the solvent and the counter-ions may play a crucial role on the ligand conformation and the M^{3+} extraction mechanism(s). It is also emphasised that small enthalpy differences may be verified with Gibbs free energy calculations in order to take in account entropy.

The present work call for further investigations concerning for example, (i) the effect of an organic solvent on terpyridines free and complexed, (ii) the description of the interaction potential (polarisation, charge transfer...), or (iii) the competition between M3+ ions and the protons for polypyridine complexation sites.

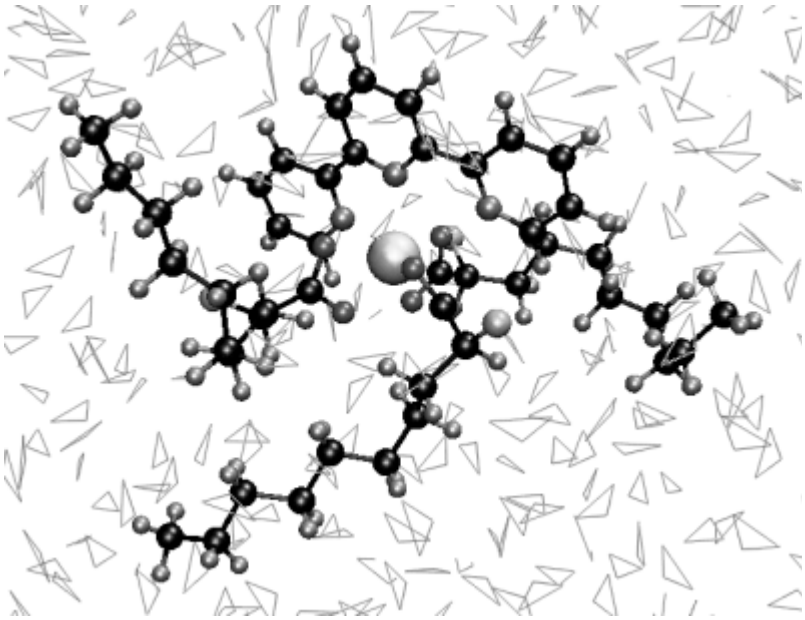

THEORETICAL AND EXPERIMENTAL STRUCTURAL STUDIES OF THE EXTRACTION OF ACTINIDES AND LANTHANIDES BY TRIDENTATE NITROGEN LIGANDS CONTAINING 1,2,4-TRIAZINES OR 1,2,4-TRIAZOLES

Michael G.B. Drew, Michael J. Hudson
Peter B. Iveson, Mark L. Russell
Department of Chemistry
University of Reading
P.O.Box 224
Whiteknights, Reading RG6 6AD
U.K.

Charles Madic
Commissariat a l'Energie Atomique
CEA-Valrhô, DCC/DRD/SEMP/SEC
30207 Bagnols-sur-Cèze Cedex
France

The separation of lanthanides and actinides by tridentate nitrogen ligands has been studied by a variety of theoretical and experimental techniques. Various oligoamines have been show to separate actinides from lanthanides in nitric acid solutions. In this work we concentrate on two ligands L^1 and L^2 that have recently been shown to have remarkable separation properties [1].

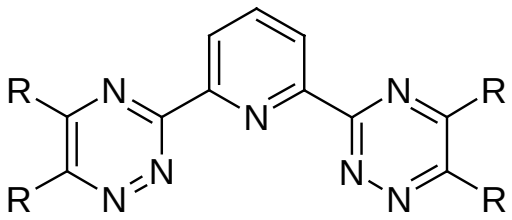

L^1

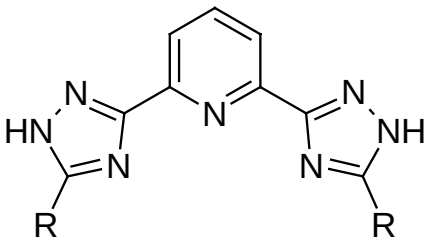

L^2

In the separation process, it has been thought that the species present at low levels of acidity are simple metal co-ordination compounds. However, our own structural studies on a number of terdentate ligands have shown a large variety of structural types which depend on the nature of the ligand and on the lanthanide concerned. In order to gain insights into the coordinative mechanism of extraction and separation, we have carried out X-ray structural studies on these two ligands with remarkable properties.

We have studied 2,6-bis(5,6-dialkyl-1,2,4-triazin-3-yl)pyridine L^1 with R = ^{i}butyl and obtained structures of the metal complexes with M = La, and Nd. The lanthanum structure contains two equivalent cations and two equivalent anions in the asymmetric unit, of formula $[La(L^1)_2(NO_3)_2]^+$ and $[La(L^1)(NO_3)_4]^-$ respectively. The two ions are 10 and 11 co-ordinate. By contrast, the neodymium structure contains two such identical cations $[Nd(L^1)_2(NO_3)_2]^+$ with $[Nd(NO_3)_4(HOEt)_2]^-$ and $(NO_3)^-$ anions. Further structural studies are in progress and show that this cation is predominant throughout the lanthanide series. While these structures have been determined with R=^{i}butyl, it seems likely that

equivalent structures are to be found with similar ligands containing different alkyl groups. The predominance of the $[M(L^1)_2(NO_3)_2]^+$ cation in the lanthanide series is consistent with our structural studies of terpyridine which show cations with this formulation are also often to be found.

We have studied 2,6-bis(5-alkyl-1,2,4-triazol-3-yl)pyridine, L^2 with R = methyl and R = butyl. The ligand with good extraction properties has R=butyl but we were unable to obtain suitable crystals of metal complexes with this ligand and so used R=methyl. However, with R=butyl we were able to obtain a crystal structure of the free ligand. There are two molecules in the asymmetric unit each with C_2 symmetry and these are interleaved surrounding a water molecule. The four triazole nitrogen atoms from two ligands are hydrogen bonded to one water molecule in a tetrahedral arrangement. The location of the hydrogen atoms on the nitrogen atoms could not be determined unequivocally in the crystal structure but it appears likely that two of the nitrogen atoms are protonated and act as hydrogen bond donors while the other two are unprotonated and act as hydrogen bond acceptors. This is supported by *ab initio* Gaussian94 calculations on the ligand which show that the hydrogen atom in the ligand is found preferentially in the 4 position but there is only a 1 kcal mol^{-1} difference when placed in the 1 position. By contrast placement in the 2 position is shown to be unlikely as the energy increases by 4.5 kcal mol^{-1}.

With R = methyl (DMTZP), we have prepared a series of metal complexes. So far, seven structures have been determined and four different structural types (A-D) have been observed (see Table 1). In each type the lanthanide is bound to only one terdentate ligand. In type A (La) the metal is bonded to one ligand, one nitrate anion and five water molecules to give a ten-co-ordinate 2+ cation. The triazole nitrogen atoms co-ordinated to the lanthanides are those in the four position. There are two further nitrates which are uncoordinated. Structures with Nd, Sm, Tb and Dy are isomorphous (type B) and show the metal ion bound to one pyridine, two triazole nitrogen atoms and also interestingly to four bidentate nitrate ions – giving a co-ordination number of eleven. There are no accompanying cations in the cell and, therefore, the charge balance must be provided by an extra proton in the triazole ligand. This is consistent with the intermolecular contacts in the unit cell which show a hydrogen bonding network with water molecules which “connect” adjacent ligands. We conclude that the exact disposition of the hydrogen atoms is disordered with any three of the four triazole nitrogen atoms being protonated in any particular ligand. It is interesting that the co-ordination number of (Nd-Dy) is 11, while that of La is only 10 despite its larger size, but this is consistent with the fact that the two monodentate water molecules take up relatively more space than the bidentate nitrate anions.

The third structural type C (Ho + Er) involves the co-ordination of three nitrogen atoms, two bidentate nitrates, one monodentate nitrate and one water molecule. It appears that the triazole rings in the nine co-ordinate complexes are doubly protonated and one of these protons is hydrogen bonded to an acetonitrile molecule. The final structural type D (Yb) shows a nine co-ordinate metal ion is bound to three nitrogen atoms and three bidentate nitrates. One of the nitrogen atoms in the protonated triazole ring is again hydrogen bonded to an acetonitrile solvent

In all these complexes, the ligands are planar and the lanthanides co-ordinate in the plane of the ligand. We have used computer modelling techniques to investigate the effect of changing the chain lengths from methyl to butyl. Starting from the crystal structures, we have increased the chain lengths from one to four carbon atoms and have established that these alkyl chains have no significant steric effect on the metal co-ordination sphere.

Table 1 : **Structure Types of DMTZP complexes established by X-ray Crystallography**

La	Ce	Pr	Nd	Pm	Sm	Eu	Gd	Tb	Dy	Ho	Er	Tm	Yb	Lu
A			B		B			B	B	C		C	D	

It will be very interesting to see whether the different structural types found for the lanthanide structures can be correlated with the extraction properties of specific lanthanides. It can be argued that there would be a wide range of structures for each lanthanide in solution and that conclusions cannot be drawn from isolated crystal structures. But in our view it seems likely that for example the large difference in structure between type B (11-co-ordination, four nitrates, protonated ligand) and C (9-co-ordination, three nitrates – one monodentate, ligand) are related to differences in structure and physical properties in solution which would significantly effect extraction properties. Work is in progress to study these complexes with EXAFS to see whether the structure types persist in solution.

Our structural studies indicate that the extraction mechanism for L^1 and L^2 is likely to be very different. The predominance of the $[M(L^1)_2(NO_3)_2]^+$ cation in the chemistry of metal complexes of L^1 is clearly significant. By contrast there is no evidence for the formation of such an ion with L^2, indeed there are no structures where the metal to ligand ratio is 1:2. It seems likely that in this case, the important factor is the formation of the $M(LH)(NO_3)_4$ neutral complex with concomitant protonation of the ligand. However for both ligands knowledge of the stoichiometry of the actinide(III) complexes is required before conclusions can be drawn again. These studies are in progress.

Acknowledgements

This work was performed with support of the Partitioning Experiments and Waste Minimisation Research Program under contract F141.CT.96-0010. "NEWPART".

REFERENCES

[1] Z. Kolarik, U. Mullich, private communication and poster, this conference (1998)

THEORITICAL AND EXPERIMENTAL STRUCTURAL STUDIES OF THE EXTRACTION OF ACTINIDES AND LANTHANIDES BY THE TRIDENTATE NITROGEN LIGAND 4-AMINO, 2,6-DIPYRDYL TRIAZINE (ADPTZ)

Michael G.B. Drew, Michael J. Hudson
Peter B. Iveson, Mark L. Russell
Department of Chemistry
University of Reading
P.O.Box 224
Whiteknights, Reading RG6 6AD
U.K.

Charles Madic
Commissariat a l'Energie Atomique
CEA-Valrhô, DCC/DRD/SEMP/SEC
30207 Bagnols-sur-Cèze Cedex
France

The separation of lanthanides and actinides by tridentate nitrogen ligands has been studied by a variety of theoretical and experimental techniques. The title ligand ADPTZ has been shown to be particularly useful in synergistic extraction systems with α-bromocapric acid. In the separation process, it has been thought that the species present at low levels of acidity are simple metal co-ordination compounds. However our own structural studies on a number of terdentate ligands have shown a large variety of structural types which depend on the nature of the ligand and on the lanthanide concerned.

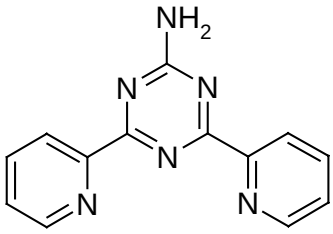

ADPTZ has been found to be produce a wide and varied structural chemistry with the lanthanide elements and this has been studied in detail via X-ray crystallography. We have prepared and studied well over 20 samples. In addition, the amino group has been acylated with cyclohexanoyl chloride to form 4-cyclohexanoylamino-2,6-dipyridyl triazine CADPTZ. The results are shown in the Table.

Table. **Crystal Structures of Lanthanide Complexes with ADPTZ**

Type	Stoichiometry	Charge	CN	Metals
1	L, 3BN, 2W	0	11	La
2	L, 3BN, 1W	0	10	La, Pr, Nd, Sm, Eu
3	L, 2BN, 3W	1	10	Nd, Sm
4	L, 2BN, 2W	1	9	Eu,Gd,Tb,Dy,Ho,Er, Tm, Yb, Lu
5	L*, 1BN, 4W	2	9	Yb
6	L, 2BN, 1MN, 1W	0	9	Yb, (Y)

L* is CADPTZ, L is ADPTZ
BN is bidentate nitrate, MN is monodentate nitrate, W is water.

The wide range of structural types found for the lanthanides with ADPTZ are evidenced in the Table. As can be seen the co-ordination number is highly dependent upon the size of the ion, but there are also variations in the preferred stoichiometry. The six structure types can be divided into two equal groups. The larger lanthanides, La-Eu, form structure types 1,2 and 3 with co-ordination numbers 11 and 10. La is the only lanthanide to form an 11-co-ordinate complex and indeed forms two different neutral complexes with an additional water molecule being the only difference between the 11 and 10-co-ordinate complexes. Both Nd and Sm form two different 10-co-ordinate complexes, one neutral with three bidentate nitrates and the other a cation with two bidentate nitrates and two water molecules. For the smaller lanthanides there are three structure types, all of which are nine-co-ordinate. The most prevalent type is the cation type 4 with two bidentate nitrates, and two water molecules. However, it is interesting that Eu forms both types 2 and 4. Variations on structure 4 are given by types 5 and 6 but these are only found with Yb and Y. These are most unusual structures as 5 contains a di cation and 6 a monodentate nitrate.

This work shows clearly that the lanthanides (and by implication the actinides) form a variety of complexes in solution and that at least some of these are cationic. It seems unlikely therefore that a single type of complex is responsible for extraction. While these solid state structures indicate that the dominant species can be predicted, there must remain some uncertainty as to the prevalent forms in solution. However, preliminary results from XAS studies provide no evidence for any variations between solid and solution structures. It is noteworthy that these six structural types represent the largest number of different structures ever found across the lanthanide series. In many other cases there are just 1 or 2 changes in co-ordination number across the series. Clearly the terdentate ligands, combined with nitrates and water, offer the potential of a wide range of stoichiometries for metal complexes.

We also report the determination of several other structures relevant to this program. These include the free 4-cyclohexanoylamino-2,6-dipyridyl triazine ligand (CADPTZ). The key feature of interest in this structure is the *cis*-*cis* conformation of the pyridine rings. This is the first time this conformation has been observed in this type of ligand in the absence of a co-ordinating metal ion or in the absence of a hydrogen bond acceptor when the ligand is in its protonated form. The reason for this is unclear but the *cis*-*cis* conformation may be stabilised via crystal packing and the formation of an intermolecular hydrogen bond between the amide hydrogen and a pyridine nitrogen atom

The structure of a corresponding Yb(III) complex of CADPTZ together with a Yb(III) complex of 4-*t*-butylacetanoylamino-2,6-dipyridyl triazine (TBADPTZ) - a ligand which was specifically made in an effort to obtain crystalline lanthanide complexes. The CADPTZ complex is interesting because there is only one bidentate nitrate co-ordinated to the Yb(III) and the co-ordination sphere is made up by four water molecules. A nitrate ion is hydrogen bonded to the NH in the amide group. In the complex with TBADPTZ. Yb(III) is co-ordinated to three nitrogen atoms, two bidentate nitrates, one monodentate nitrate and one water molecule. Attempts were also made to prepare Sm(III) and Nd(III) complexes with these ligands but in each case the amide bond was found to hydrolyse and the corresponding Ln/ADPTZ complexes were isolated as crystalline products. The stability of Ln/TBADPTZ complexes in solution is currently being studied by proton NMR.

The structures of a complex formed between Nd(III) and an ADPTZ analogue - 4-amino-2,6-di(4-methylpyridyl)-triazine (ADMPTZ) has also been determined. The methyl groups were added to increase the hydrophobicity of the ligand. This structure is consistent with one of the previously determined Nd/ADPTZ structures - the Nd(III) being co-ordinated to 3 pyridyl nitrogen atoms, three bidentate nitrates and one water molecule.

This work suggests that the extraction process with terdentate planar nitrogen-donor ligands is extremely complicated. The lanthanides can form many different types of complexes and we are as yet uncertain as to the types of complexes formed with the actinides. Further work is clearly needed to elucidate the extraction mechanisms.

Acknowledgement

This work was performed with support of the Partitioning Experiments and Waste Minimisation Research Program under contract F141.CT.96-0010. “NEWPART”.

OXIDATION OF AMERICIUM IN NITRIC MEDIA: A MECHANISTICAL STUDY

D. Chartier, L. Donnet, S. Picart, J. M. Adnet
CE/Valrho/Marcoule
CEA/DCC/DRRV/SPHA
BP 171
30207 Bagnols-sur-Cèze Cédex,
France

Abstract

One of the alternatives selected by CEA for the partitioning of minor actinides from solutions containing fission products is the selective extraction of oxidised americium. This is the SESAME process (Selective Extraction and Separation of Americium by Means of Electrolysis) under development in the ATALANTE facility. This paper presents the study of the mechanism of americium oxidation in nitric media. Oxidised americium is produced though the use of heteropolyanionic ligands such as phosphotungstate or silicotungstate and electrogenerated Ag^{2+}.

The first part of this work shows the existence of the lacunary heteropolynion (LHPA) complex with americium (stoechiometry 1:1) whose β_1 and k_2 constants have been estimated. Those results enable us to determine the conditional redox potential of Am(IV)/Am(III) pair in the presence of LHPA ligands and to explain the different behaviour of the two heteropolyanions during electrolysis. The second part of this study concerns the Am(IV)/Am(V) transition. Raman spectroscopy studies would prove that the only oxidable species is the 1:1 Am(IV) complex. According to the previous results, a modelisation of americium electroxidation has then been performed and is in good agreement with experimental results.

Eventually the Am(VI)/Am(V) step was investigated to improve a selective analysis of americium oxidation states. A method has been developed to follow the americium concentration during extraction process.

SELECTIVE EXTRACTION OF CE(IV) AS A FIRST STEP OF THE SESAME PROCESS

N. Faure, L. Donnet, J.M. Adnet
CE/Valrho/Marcoule
CEA/DCC/DRRV/SPHA
BP 171
30207 Bagnols-sur-Cèze Cédex,
France

Abstract

SESAME process (selective extraction of americium by electrochemical method) is developed in the frame of the French SPIN programme (separation and incineration) whose main goal is the recovery and transmutation of minor actinides and long-lived fission products contained in the spent nuclear fuel. Depending on the flow sheet option, americium could be separated from curium (SESAME A process), from curium and lanthanides (B route) or from a PUREX raffinate (C route). Main studies are underway on the SESAME B process.

Am(III) is oxidised into Am(VI) in the presence of silver nitrate and lacunary heteropolyanion, and then extracted by tributyl phosphate (TBP). Concerning the B and C routes, the feed solutions contain cerium which is totally complexed by polyanion. As the concentration of lanthanides is 13 times higher than that of americium, the polyanion consumption could be dramatically lowered by previously removing the cerium from the feed solution. Selective extraction of cerium before americium oxidation and extraction has thus been studied on inactive solutions containing only cerium, lanthanum, neodymium and europium. Their concentrations have been chosen equal to that of a PUREX raffinate of an UOx1 spent fuel, concentrated 10 times.

After a complete oxidation of Ce(III) into Ce(IV) in 5 M nitric acid, its extraction by 50 vol % TBP in dodecane is carried out in a set of 2 or 4 centrifugal contactors. An oxidising aqueous scrubbing in the organic phase (AgO in 5 M nitric acid) is performed in 2 additional centrifugal contactors to improve the selectivity of the cerium extraction towards other lanthanides. Finally, the cerium stripping is achieved by using a reducing solution of hydroxylamine nitrate in 1 M nitric acid.

The tested solutions have been treated on line by using 2 sets of 4 centrifugal contactors. More than 99 mol % of cerium was extracted with less than 0.5 wt % of other lanthanides.

DECOMPOSITION OF OXALATE PRECIPITATES BY PHOTOCHEMICAL REACTION

Jae-Hyung Yoo and Eung-Ho Kim
Korea Atomic Energy Research Institute P.O. Box 105
Yusong, Taejon, 05-600,
Korea

Abstract

A photo-radiation method was applied to decompose oxalate precipitates so that it can be dissolved into dilute nitric acid. This work has been studied as a part of partitioning of minor actinides. Minor actinides can be recovered from high-level wastes as oxalate precipitates, but they tend to be co-precipitated together with lanthanide oxalates. This requires another partitioning step for mutual separation of actinide and lanthanide groups. In this study, therefore, some experimental work of photochemical decomposition of oxalate was carried out to prove its feasibility as a step of partitioning process. The decomposition of oxalic acid in the presence of nitric acid was performed in advance in order to understand the mechanistic behaviour of oxalate destruction, and then the decomposition of neodymium oxalate, which was chosen as a stand-in compound representing minor actinide and lanthanide oxalates, was examined. The decomposition rate of neodymium oxalate was found as 0.003 mole/hr at the conditions of 0.5 M HNO_3 and room temperature when a mercury lamp was used as a light source.

Introduction

Since minor actinides such as americium and curium, and lanthanides, in general, have similar chemical properties in long-lived radionuclide partitioning processes, it is not so easy to separate minor actinides selectively from other elements. Instead, it is a typical way to separate both of them from other elements in the first step and then to separate them from each other in the next step. Oxalate precipitation, therefore, is an applicable way for the first step because minor actinide oxalates can be coprecipitated with lanthanide oxalates (Forsberg , 1980). The mixture of minor actinides and lanthanides should then be processed for mutual separation, requiring that the oxalates precipitated should be dissolved into a solution for subsequent processing. In this study, the photochemical method was used to test the feasibility of oxalate decomposition and its dissolution in nitric acid. At first, photo-decomposition of oxalic acid was carried out to investigate the mechanistic behaviours of the oxalate ion decomposition in the presence of nitric acid, and then the decomposition of neodymium oxalate was examined under the same conditions.

Experimental

Experimental equipment and procedure

The photo-radiation equipment (Model : RPR-208) with eight 15 ml reaction tubes made of quartz and eight mercury lamps (120 W, 2573 Å of wavelength) was used in the experiments. As shown in Figure 1, mercury lamps are located around reaction tubes, emitting UV light toward the tubes which were placed at the circumference of the circular horizontal acryl supporter so that simultaneous irradiation for the tubes can be achieved. In order to suppress the temperature increase in the solution of reaction tubes during irradiation, cooling air is blown up into the air-ports installed at the bottom of reactor. In every run of experiments, the volume of working solution in the reaction tubes was set to 10 ml and 0.01-0.1 ml of a sample was periodically taken to determine the oxalic acid concentration of the solution during the photolysis.

Figure 1. **Schematic diagram of the photolysis system**

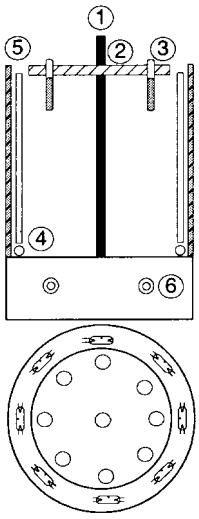

1. Vertical supporter
2. Horizontal acrylic supporter
3. Sample tube
4. Aeration port
5. Hg-Lamp
6. Power generator

Chemical analysis

The light absorptions of pure nitric acid and oxalic acid in 0.5M nitric acid were scanned by UV spectrophotometer (Model : Shimadzu UV-160A) in order to confirm the applicability of the mercury

lamp to our workscope of photolysis. During the photolysis, the decomposed fraction of oxalic acid was determined by measuring COD (Chemical Oxygen Demand) of the solution by means of Hack 2000 DR-type COD analyser, and the concentration of NO_2^- ion produced from nitric acid was determined by reflectometry (Reflectoquant, Merck).

Result and discussion

Photo-decomposition of oxalic acid

Figure 2.

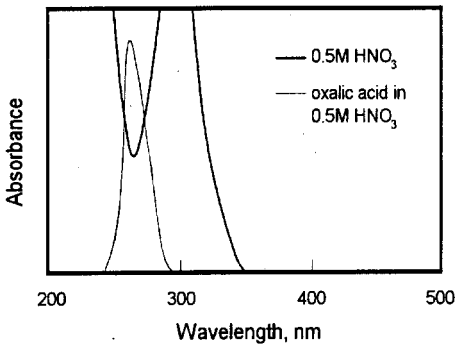

Figure 3.

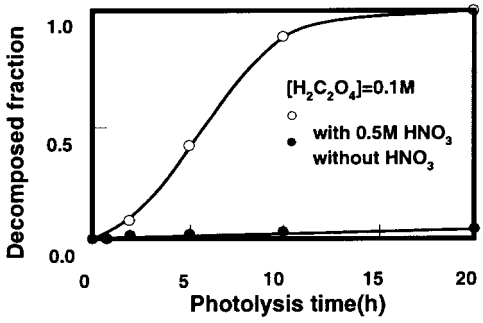

Figure 2 shows UV spectrums of two solutions; one for 0.5 M nitric acid and the other for the mixture of 0.1 M oxalic acid and 0.5 M nitric acid. It illustrates that oxalic acid has an absorption peak around the wavelength of the mercury lamp. However, as shown in Figure 3, the decomposition rate of oxalic acid in the absence of nitric acid was very low compared with that in the presence of nitric acid indicating that the role of nitric acid should be enormous in the decomposition of oxalic acid. Experimental results show that the decomposition yield of oxalic acid without nitric acid is less than 5% even after 20 hrs irridiation, whereas 0.1 M oxalic acid in 0.5 M nitric acid was completely decomposed within 20 hr. In order to search the role of nitric acid, a solution containing only nitric acid was first irradiated in the photochemical reactor. The results, as illustrated in Figure 4 gives that the content of nitrite ion increases with nitric acid concentration and also with irradiation time. According to F. Barat et al (1970) and P. Warneck et al (1988), the photolysis of nitrate ions involves two pathways as illustrated in Eqn (1)-(3). On the basis of these phenomena, the photolysis mechanism of nitric acid has been known as:

1. $NO_3^- + h\nu \rightarrow NO_2^- + O$
2. $NO_3^- + h\nu \rightarrow NO_2^{\cdot} + O^{\cdot -}$
3. $O^{\cdot -} + H_2O \rightarrow {}^{\cdot}OH + OH^-$
4. $NO_2^{\cdot} \rightarrow N_2O_4$
5. $N_2O_4 + H_2O \rightarrow NO_2^- + NO_3^- + 2\,H^+$
6. $NO_2^- + h\nu \rightarrow NO^{\cdot} + O^{\cdot -}$
7. $NO_2^- + {}^{\cdot}OH \rightarrow NO_2 + OH^-$

Accordingly, it can be inferred that the photo-decomposition of oxalate in a nitric acid medium will be induced by the oxidants such as NO_2^- ion and ${}^{\cdot}OH$ radical as follows:

8. $H_2C_2O_4 + 2\,NO_2^- \rightarrow 2\,NO + 2\,CO_2 + 2\,OH^-$
9. $H_2C_2O_4 + 2\,OH \rightarrow 2\,H_2O + 2\,CO_2$

Figure 4. **Effect of nitrate concentration on nitrite formation during photolysis**

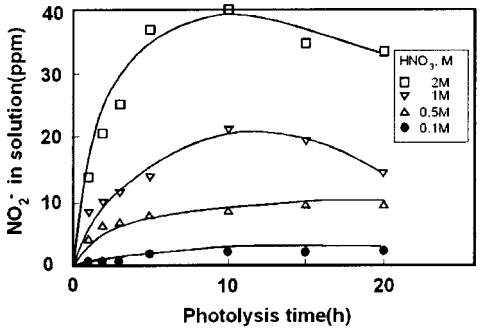

Warneck and Wurzinger (1988) ,however, reported that the quantum yield of ·OH formation from nitric acid is much higher than that of the other pathway, and therefore oxidations are generally attributed to hydroxyl radicals which are more reactive than atomic oxygen.

In our experiments, the effect of nitric acid concentration on the destruction of oxalic acid was examined at first. The maximum decomposition fraction was obtained when the nitric acid concentration is around 0.5 M and the decomposition fraction was rather decreased above 0.5 M as shown in Figure 5. This result indicates that the major contributor to the destruction of oxalate ion is not the nitrite ion because more nitrite ions are generated as the nitrate concentration becomes higher, as shown in Figure 4 and Figure 6. The results in Figure 4 are obtained when there is no oxalic acid contained in the nitric acid whereas those results in Figure 6 are gained when 0.1 M oxalic acid is put into the nitric acid. In this study, therefore, it was considered that the reaction in Eqn (9) would be more dominant than that in Eqn (8) in the photo-decomposition of oxalic acid, that is, the following phenomena would be expected: if more ·OH is consumed by the oxalic acid, then its content will be reduced, resulting in less consumption of NO_2^- ion in the reaction of Eqn (7), and therefore the NO_2^- concentration will grow as more oxalic acid is added into the nitric acid. Finally, this inference was proved by the experimental results in Figure 7. When the nitric acid concentration increases above 0.5 M, then the reaction in Eqn (7) will become more active because more nitrite ions generated from the nitric acid consume hydroxyl radicals, which will certainly reduce the oxalate decomposition yield. Figure 8 shows the whole pathways of the photolysis of nitrate ion in the decomposition procedure of oxalic acid.

Figure 5. **Effect of nitrate concentration on photo-destruction of oxalic acid**

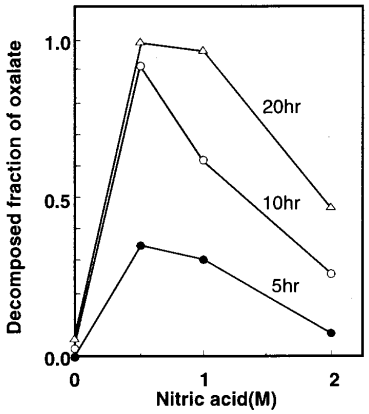

Figure 6. **Effect of nitrate concentration on nitrite formation in the presence of oxalic acid**

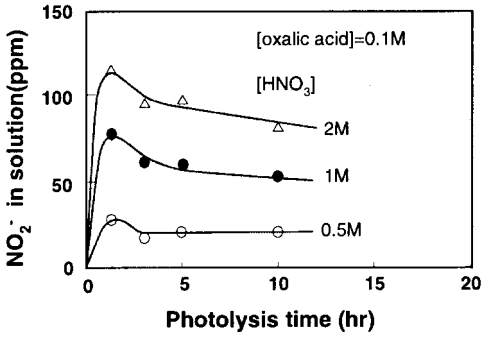

Figure 7. **Effect of oxalic acid concentration on the rate of nitrite formation during photolysis**

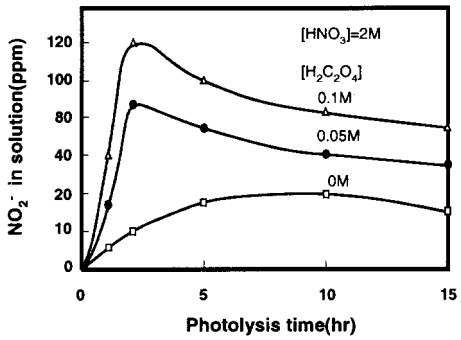

Figure 8. **Pathways for photolysis of nitrate and nitrite**

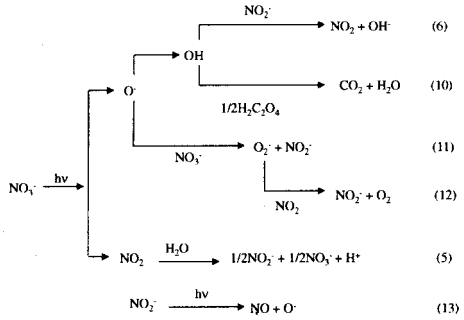

Photo-decomposition of oxalate salt

Since the decomposition of oxalic acid is mainly induced by a hydroxyl radical, oxalate salts are also inferred to be destructed by the same mechanism, that is, neodymium oxalate will be decomposed by the following mechanism:

$$10.\ Nd_2(C_2O_4)_3 + 6\,^{\cdot}OH + 6\,H^+ \rightarrow 2\,Nd^{3+} + 6CO_2 + 6\,H_2O$$

In our experiments, the decomposition rates were compared between oxalic acid and neodymium oxalate for the same content of oxalate. The result in Figure 9 shows that the decomposition rate of oxalate salt is slightly slower than that of oxalic acid. This is due to the fact that oxalate salt, which exists as a solid, needs additional time to dissolve into the solution, retarding the destruction process. In order to obtain the decomposition rate, various contents of neodymium oxalate were dissolved in 0.5 M nitric acid and duration times for complete dissolution were measured. As a result, the time increases linearly with the quantity of initial neodymium oxalate, as shown in Figure 10, giving the dissolution rate of 0.003 mole/hr at the condition of 0.5 M nitric acid and room temperature. Consequently, the final concentration of nitric acid can be diminished to less than 0.1 M in the solution due to the destruction of the nitrate ion, which would then give an appropriate condition to separate minor actinides and lanthanides from each other. Such partitioning processes as ion exchange and solvent extraction, which require very low acidity of feed solution, can be applied for the purpose of mutual separation.

Figure 9. **Decomposition rates of oxalic acid and neodymium oxalate during photolysis**

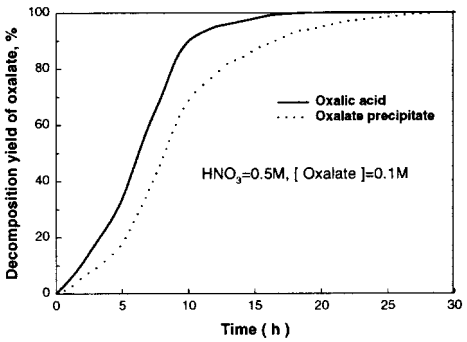

Figure 10. **Complete decomposition time of neodymium oxalate with its initial concentration**

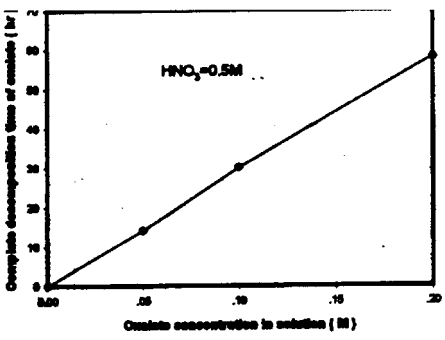

Conclusion

The mechanism of oxalate decomposition in nitric acid was experimentally investigated in this study and it was elucidated that the decomposition reaction is dominated by the reaction of oxalic acid with hydroxyl radical generated from the nitric acid, rather than with the nitrite ion which is also produced from the nitric acid. The maximum decomposition rate of oxalic acid with the mercury lamp (λ = 254 nm) was obtained when the nitric acid concentration is about 0.5 M in the initial solution. This phenomenon is interpreted as that, at lower nitric acidity, less hydroxyl radical is generated from nitric acid, reducing the oxalate destruction yield, however, a larger quantity of the nitrite ion forms at higher acidity, consuming more hydroxyl radicals and thus diminishing the oxalate decomposition yield.

Acknowledgements

This project has been carried out under the nuclear R&D program of the Korean MOST.

REFERENCES

[1] Daniels *et al.,* Photochemistry of the Aqueous Nitrate System J. Physical Chemistry, 72(2), 389-399 (1965).

[2] Forsberg C. W., Separation of Americium,Curium, and Tri-valent Lanthanides from High-Level Wastes by Oxalate Precipitation Nuclear Technology, 49, 243-252 (1980).

[3] Sarakha *et al.,* Phototransformation of 2-Phenyl phenol induced in Aqueous Solution by Excitation of Nitrate Ions J. Photochem. Photobiol. A: Chem., 75, 61-65 (1993).

[4] Shuali *et al.,* On the Photochemistry of Aqueous Nitrate Solutions Excited in the 195 nm Band, J. Phys. Chem.,73(10),3445-3451 (1969).

[5] Brat. L. Gilles, B. Hickel and J. Sutton, J. Chem.Soc. A ,1982 (1970).

[6] Warneck and C. Wurzinger, J. Phys. Chem.,92, 6278 (1988).

[7] Franck Machado and Pierre Boule, J. Photochem and Photobio A: Chemistry 86, 73-80 (1995).

SYSTEMATIC UNCERTAINTIES ON MONTE CARLO SIMULATION OF LEAD BASED ADS

M. Embid
CIEMAT. Fission driven by Accelerator and Isotopes Transmutation
Avda. Complutense, 22 Edif.-17 Dpcho.101, 28040 Madrid
Spain

R. Fernández
CIEMAT. Fission driven by Accelerator and Isotopes Transmutation
Avda. Complutense, 22 Edif.-17 Dpcho.101, 28040 Madrid
Spain

J.M. García-Sanz
CIEMAT. Fission driven by Accelerator and Isotopes Transmutation
Avda. Complutense, 22 Edif.-55, 28040 Madrid
Spain

E. González
CIEMAT. Fission driven by Accelerator and Isotopes Transmutation
Avda. Complutense, 22 Edif.-17, 28040 Madrid
Spain

Abstract

Computer simulations of the neutronic behaviour of ADS systems foreseen for actinide and fission product transmutation are affected by many sources of systematic uncertainties, both from the nuclear data and by the methodology selected when applying the codes. Several actual ADS Monte Carlo simulations are presented, comparing different options both for the data and for the methodology, evaluating the relevance of the different uncertainties.

Introduction

This report shows a compilation of several exercises to evaluate sources of the systematic uncertainties on the predictions computed on ADS Montecarlo simulations, including:

A. Uncertainties in the estimation of K_{eff} of a lead based ADS from the nuclear cross section libraries: ENDF-BVI.4 vs. JENDL-3.2.

B. Sensitivity study for the K_{eff} of a lead based ADS on different proton beam window heights

C. Comparison of the fully detailed heterogeneous geometrical descriptions of a lead based ADS versus its simplified homogeneous description in MC neutronic calculations.

D. Sensitivity studies on lead based ADS with UO_2 fuel.

E. Sensitivity study on the spatial segmentation of lead based ADS geometry for burnup evolution simulation

A. Uncertainties in the estimation of K_{eff} of a lead based ADS from the Nuclear Cross Section Libraries: ENDF-BVI.4 vs. JENDL-3.2

In any simulation of the neutronic behaviour of a nuclear system, the accuracy of the results is limited by the precision of used nuclear databases, in particular for the cross sections. In the study of Accelerator Driven System (ADS) for transmutation, new elements in nuclear systems appear. The best example is the very important role played by unusual isotopes, particularly lead and some transuranids. In the present paper, the results of a comparison of the predicted behaviour of one Th-TRU and lead based ADS according to the ENDFB-6.4 and JENDL-3.2 databases will be presented.

The studied ADS configuration is based on: liquid lead coolant with natural convection, Th+TRU fuel and a thermal power of 250 MWth. For this study a simplified ADS model intended for TRU incineration has been selected. The main characteristics are: the use of a mixture of ThO_2 and transuranids dioxide as fuel and lead as cooling and diffusory material. More details on, fuel and geometrical parameters can be found in references [1,2].

K_{eff} dependence on the cross section database

For the ADS described in the previous paragraph, K_{eff} has been computed using the “kcode” module of the MCNP-4b [3] Monte Carlo code.

Three groups of simulations have been computed, each one corresponding to a different cross section database set. In case 1, the ENDFB-6.4 cross section has been used for all the isotopes, translated to ACE format using NJOY94.61 [4], at 750 K for the lead and at 1200 K for all the other isotopes. In case 2, the JENDL-3.2 cross sections are used for all the isotopes, also computed with the help of NJOY94.61 and at same temperatures as in case 1.

The third case is subdivided in several subcases, at each subcase the JENDL-3.2 cross sections database is used for all the isotopes except one or several isotopes. Table 1 describe the details of each case. In this way the individual effects of the Pb, ^{240}Pu, ^{239}Pu, ^{232}Th and Fe cross sections and the combined effects of Pb and ^{240}Pu on K_{eff} have been studied.

For each simulation, the K_{eff} value has been computed using the kcode module of MCNP-4b, running 50 cycles of 2000 fission neutrons each. The K_{eff} estimators were computed over the last 45 cycles, skipping the events of the first five. The starting fission source is given by a SRCTP file produced in a previous MCNP-4b run using the same input file. At the end of each run, MCNP checks that every cell containing fissile material has been sampled.

Table A-1. **Simulated cases with MCNP-4b**.

Case	Isotope	New Library	Temp. (^{0}K)
1	All	ENDFB-6.4	-
2	All	JENDL-3.2	-
3.1	All JENDL3.2 except Pb nat.		
	^{206}Pb (24.44%)	ENDFB-6.4	750
	^{207}Pb (22.42%)	ENDFB-6.4	750
	^{208}Pb (53.14%)	ENDFB-6.4	750
3.2	All JENDL3.2 except		
	Pb-isotopic mixture	ENDFB-6.4	750
	^{240}Pu	ENDFB-6.4	1200
3.3	All JENDL3.2 except ^{240}Pu	ENDFB-6.4	1200
3.4	All JENDL3.2 except ^{232}Th	ENDFB-6.4	1200
3.5	All JENDL3.2 except ^{239}Pu	ENDFB-6.4	1200
3.6	All JENDL3.2 except Fe-nat		
	^{54}Fe (5.84%)	ENDFB-6.4	1200
	^{56}Fe (91.75%)	ENDFB-6.4	1200
	^{57}Fe (2.12%)	ENDFB-6.4	1200
	^{58}Fe (0.28%)	ENDFB-6.4	1200

The final K_{eff} selected is a statistical combination [3] of three individual estimators: collision, absorption and track-length. The values of the different estimators and the final combined result for K_{eff} in the different cases studied are shown in table A-2.

Table A-2 **Value of the K_{eff} in each studied case**

	K_{eff} estimators				
Case	**$K_{coll.}$**	**$K_{abs.}$**	**K_{tl}**	**K_{eff}**	**Standard deviation**
1	0.9606	0.9609	0.9607	0.9607	0.002
2	0.9445	0.9445	0.9454	0.9444	0.002
3.1.	0.9670	0.9699	0.9672	0.9677	0.002
3.2.	0.9708	0.9667	0.9710	0.9692	0.002
3.3.	0.9441	0.9441	0.9440	0.9441	0.002
3.4.	0.9349	0.9364	0.9344	0.9349	0.002
3.5.	0.9401	0.9377	0.9404	0.9392	0.001
3.6.	0.9408	0.9405	0.9411	0.9409	0.002

A large difference, 0.016 ± 0.003, is observed in the predicted value of K_{eff} using ENDF (case 1) versus JENDL (case 2) libraries. This difference would induce a 30% difference in the neutronic multiplication. The largest contribution come from lead, cases 3.1 and 3.2. In fact the ENDF databases for lead alone will produce an even larger difference, 0.023 ± 0.003. This difference is slightly compensated by the ^{232}Th cross sections, case 3.4. Changing the ^{239}Pu, ^{240}Pu or Fe cross sections databases, the calculated K_{eff} is not modified significantly. In the following paragraphs the difference on the lead cross sections are analysed in order to identify the origin of the discrepancy in the K_{eff} estimation.

Main lead cross sections (JENDL-3.2 and ENDFB-6.4).

Total, elastic, inelastic, (n,2n), (n,3n) and capture, the more relevant cross sections for lead, are shown in figure A-1.

There are very small differences on total, elastic scattering and capture cross sections of lead between the two libraries, JENDL-3.2 and ENDFB-6.4. On other hand, there are significant differences on the (n,2n) and (n,3n) cross sections but only for energies above 10 MeV.

The largest differences appear on the inelastic scattering reactions. Due to its large cross section between 1 and 10 MeV, the inelastic reactions are the dominant non-elastic process at these energies. In this range the values provided by JENDL-3.2 are always higher than the corresponding to ENDFB-6.4, figure A-2, for all the lead isotopes. In addition secondary neutrons energies are computed with different algorithms.

Figure A-1. **Main neutron cross sections for natural lead (JENDL-3.2).**

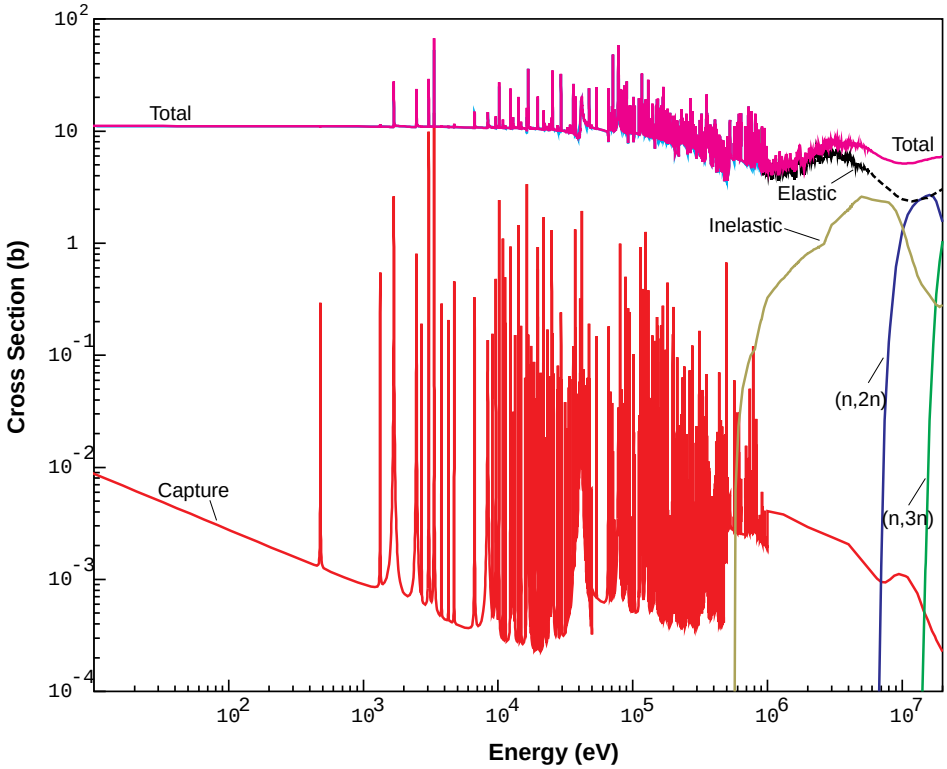

Figure A-2. **Inelastic-scattering cross section for ^{208}Pb and ^{207}Pb (JENDL-3.2 - ENDFB-6.4)**

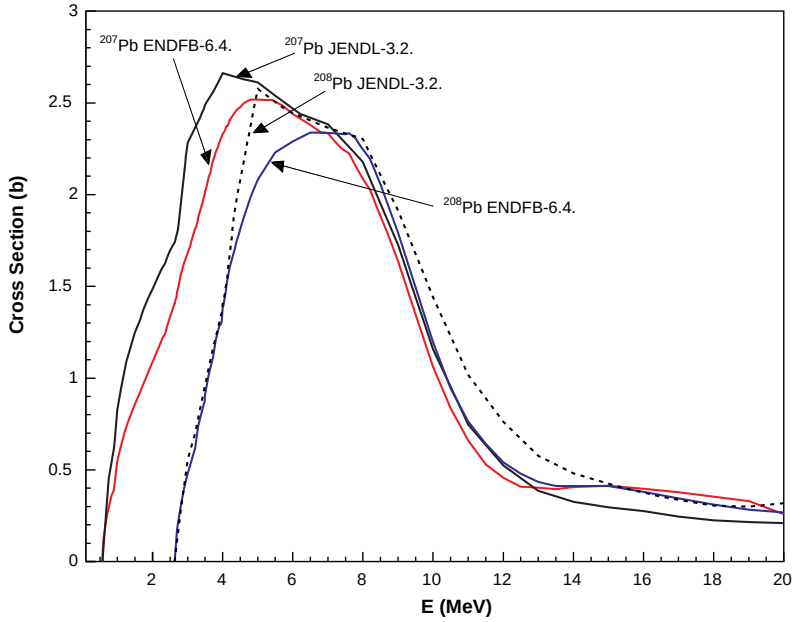

Analysis of the results.

According to the previous section and taking into account the neutron flux energy spectra, the largest differences should come from the inelastic scattering cross section of lead. In figure A-3 two graphs are shown: the average neutron fluences and the inelastic-scattering cross sections of core material, for the two libraries. Figure A-4 displays the ratios between both nuclear databases for the graphs of figure A-3.

Figure A-3. **Differences on the average core neutron fluence and on the inelastic cross section for JENDL-3.2 versus ENDFB-6.4**

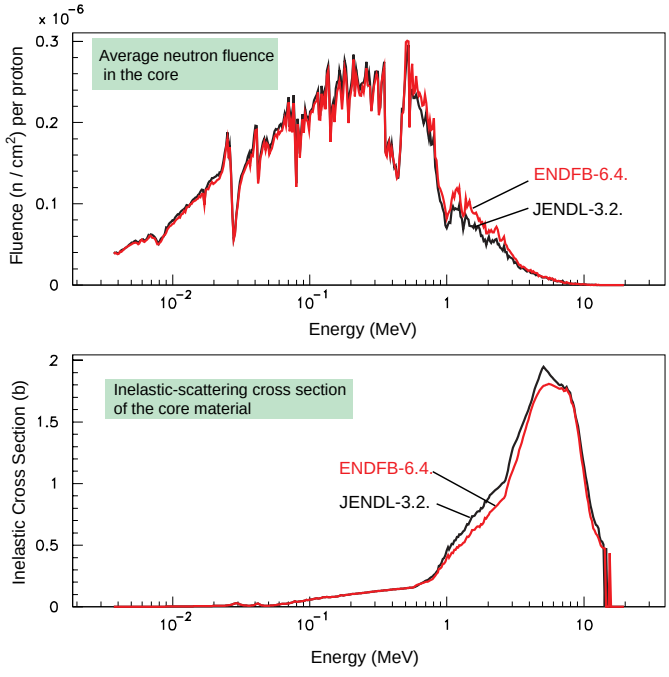

Figure A-4. **Ratios of the comparisons JENDL-3.2 versus ENDFB-6.4 of the previous figure**

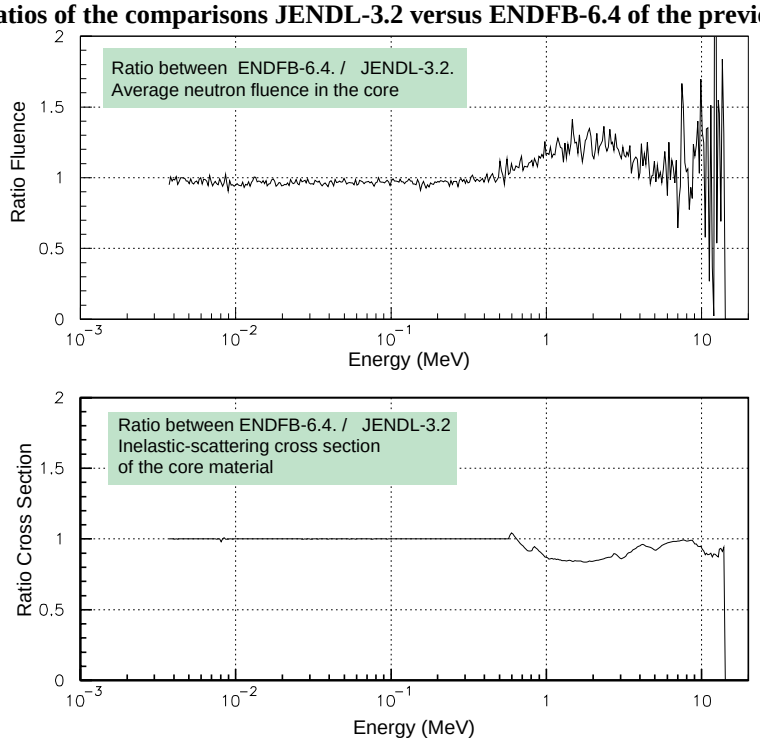

The conclusion from the last figures is that the higher inelastic scattering rate predicted by the JENDL-3.2 database sends more neutrons, from the energy range between 500 keV and 20 MeV, directly to lower energies. Figure A-5 shows that for the Th+TRUs mixture of the ADS core, fission dominates clearly over capture in that energy range whereas capture dominates over fission at lower energies, for both databases. The obvious result is that a larger fission rate and consequently a larger K_{eff} are predicted by ENDF.

Figure A-5. **Capture, fission and inelastic-scattering cross sections for the ADS core material with both libraries**

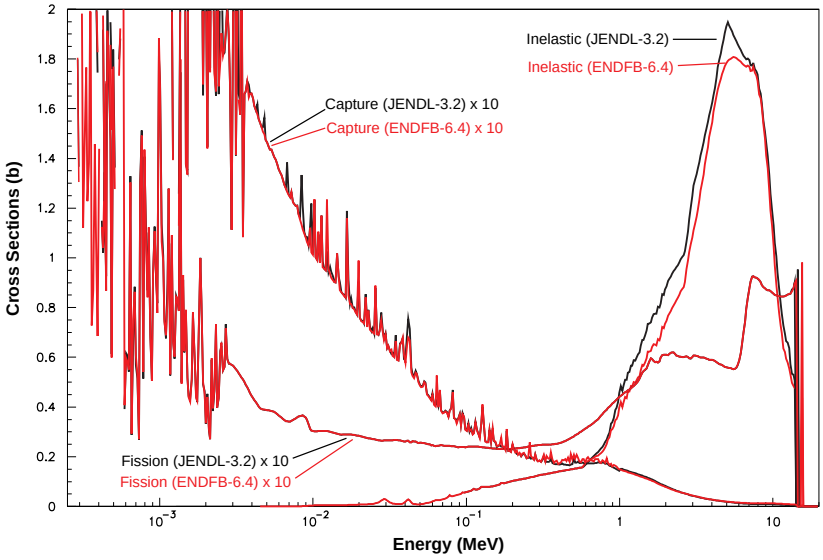

Evaluated versus experimental cross section data

The figure A-6 shows the comparison between the evaluated inelastic-scattering cross section by both nuclear databases and the EXFOR-97 [5] experimental data (non-elastic cross-sections).

The data available are clearly insufficient for making a choice. It should be noted, however, that experimental points not available in EXFOR-97 have been used in both the JENDL-3.2 and the ENDFB-6.4 evaluations.

Figure A-6 **Evaluated inelastic scattering cross section of lead from JENDL-3.2 and ENDFB-6.4 versus experimental data (EXFOR-97)**

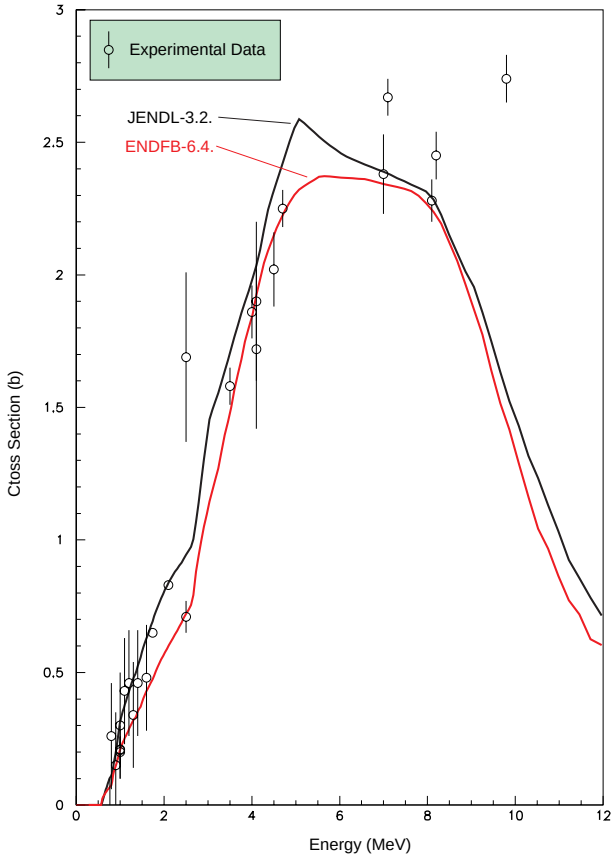

Conclusions of exercise A

According to JENDL-3.2 database the inelastic scattering with lead sends more neutrons, from the energy range between 500 keV and 20 MeV, directly to lower energies, than in simulations using ENDF-BVI.4. Fission dominates clearly over capture in the high energy range whereas capture dominates over fission at lower energies, for both databases. The obvious result is that a larger fission rate and consequently a larger K_{eff} are predicted by ENDF.

Unfortunately the available experimental data do not appear to be sufficient to make a clear choice. In the present situation this uncertainty has to be taken into account in the predictions of lead based ADS.

On the other hand it would be very interesting to have extra experimental data to enable more precise evaluations.

B. Sensitivity study for the K_{eff} of a lead based ADS on different proton beam window heights

The performance of an Accelerator Driven System (ADS), is conditioned by the optimisation of the geometrical coupling between the accelerator and the subcritical nuclear assembly. The aim of this exercise is to study the sensitivity to this parameter and to find an optimisation for a given ADS configuration. In the exercise [7], the position (height) of the beam window respect to the subcritical device core is modified in a large range. The other parameters of the ADS remain fixed.

The ADS set-up correspond to the case described in the references [2,3], but with a variable height of the beam window respect to the subcritical device core. These references also describes the MCNP and libraries versions used to simulate the neutron transport below 20 MeV. The proton beam interaction with lead, the neutron production by spallation and the transport of these neutrons down to 20 MeV is done with the help of LAHET [6].

In all the cases considered the protons in the beam have a kinetic energy of 400 MeV. In the exercise, the window height has been varied from -30 cm (down) to 60 cm (up) respect for the centre of the subcritical device core. Figure B-2 shows the neutron multiplication constant, K_s, for the different positions of the beam window. In all cases the neutron source is defined as the set of neutrons produced by the proton beam, stopped as soon as the neutron energy is smaller than 20 MeV. A wide flat region is observed between 5 cm and 35 cm above the centre of the subcritical device core. Outside this region, the K_s decreases.

Figure B-1. **Side view of the ADS. Searching of the optimal height of the neutronic spallation source**

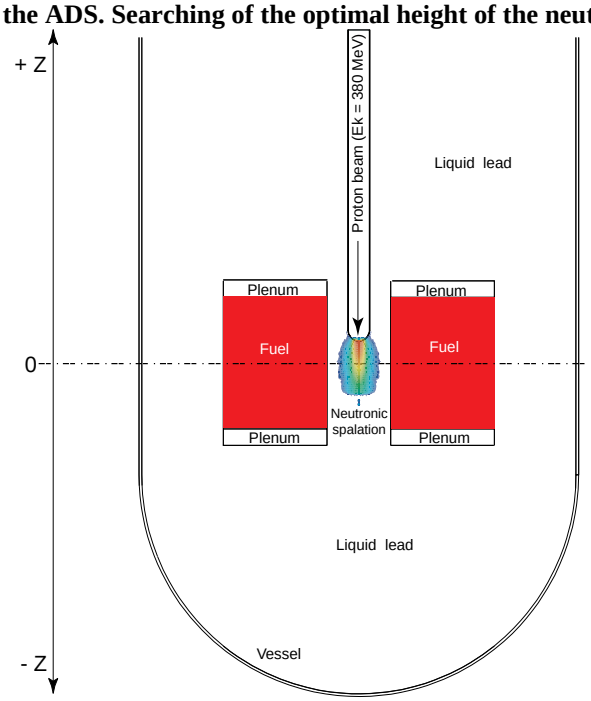

Figure B-2 **K_s variation versus the height of the beam window respect to the core centre**

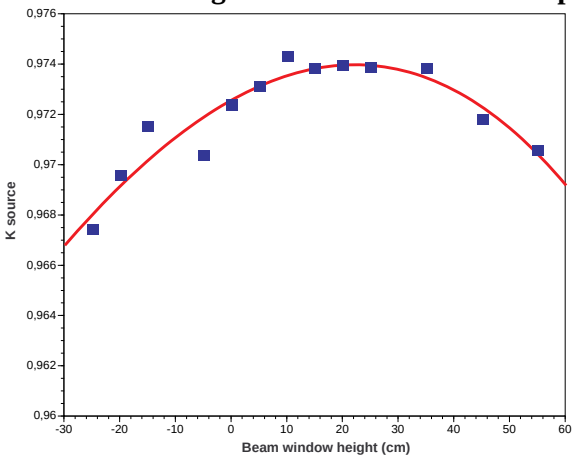

C. Comparison of the fully detailed heterogeneous geometrical descriptions of a lead based ADS versus its simplified homogeneous description in MC neutronic calculations

The need of computer time reduction in the Montecarlo (MC) simulations and the fact that the mean collision length is larger than the distance between pins in the typical accelerator driven subcritical fission device, ADS, has leaded to use homogeneous approximations of the detailed geometry in many studies of this type of devices.

In this paper two geometry models, from a larger study [8,9] of the EA-1500 (Energy Amplifier of 1500 MWth) have been compared:

1. A complete geometry definition of each fuel pin (including plenums, cladding and void) (Heterogeneous model).
2. Homogeneous mixture of the material of each bundle, distributed over its complete volume.

All the simulations were performed with the help of MCNP4b for the neutron transport and evaluation of the criticality of the system. LAHET was used when it was necessary to simulate the interaction of the protons from the accelerator with the spallation target. The main characteristics of the fuel bundles of the ADS for this study are shown in table C-1 and the core geometries as presented in figures C-1 and C-2.

Table C-1 **Main Characteristics of the fuel bundles**

	Inner Core	**Outer Core**	**Breeder**
Flat to flat (mm)	234	234	234
Thickness of the wall bundle (mm)	3	3	3
Distance between fuel pins (mm)	12.43	11.38	11.38
Number of bundles	30	90	42
Number of fuel pins in a bundle	331	397	397
Material of the wall bundle	HT9	HT9	HT9
Coolant/Moderator	Pb	Pb	Pb
Fuel Composition	ThO_2+UO_2	ThO_2+UO_2	ThO_2

Figure C-1. **Top view of the homogeneous EA-1500 core**

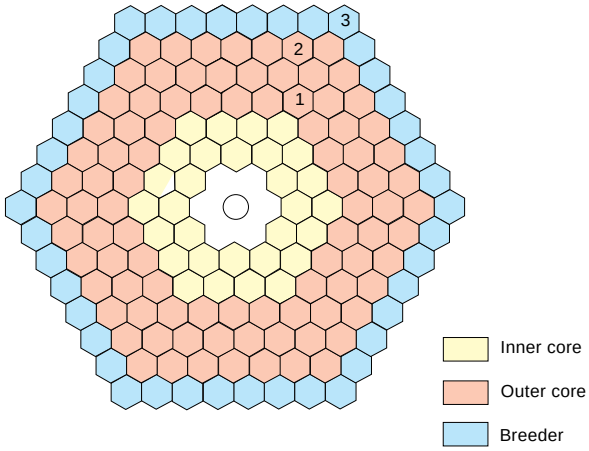

Figure C-2. **Full detailed geometry (Heterogeneous model) of the simulated ADS by MCNP-4b. The differences in the neutron energy distribution of the fluence for the heterogeneous and homogeneous model are shown in figure C-3 and C-4 as function of the energy**

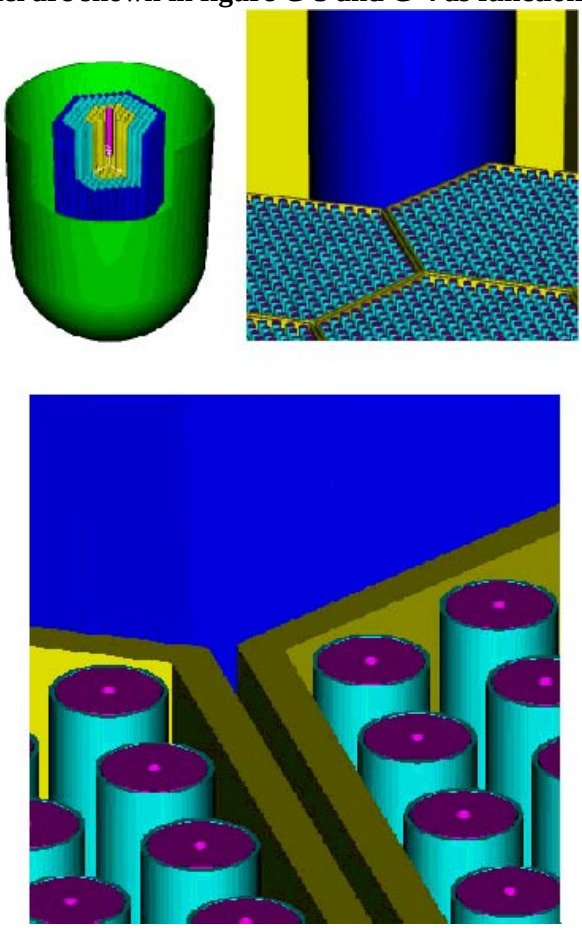

Figure C-3 **Homogeneous / heterogeneous fuel fluences: Inner core**

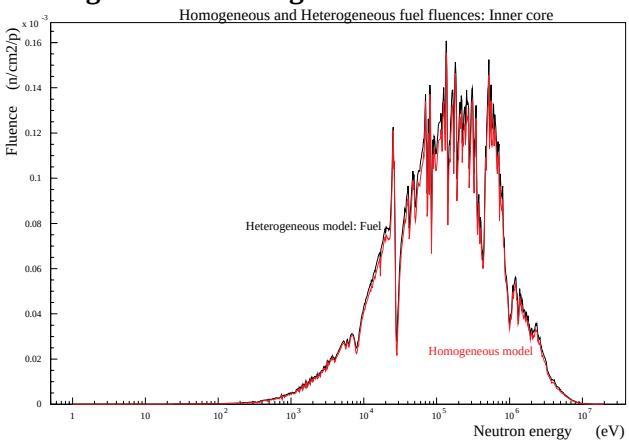

Figure C-4 **Homogeneous / heterogeneous fuel fluences ratio: Inner core**

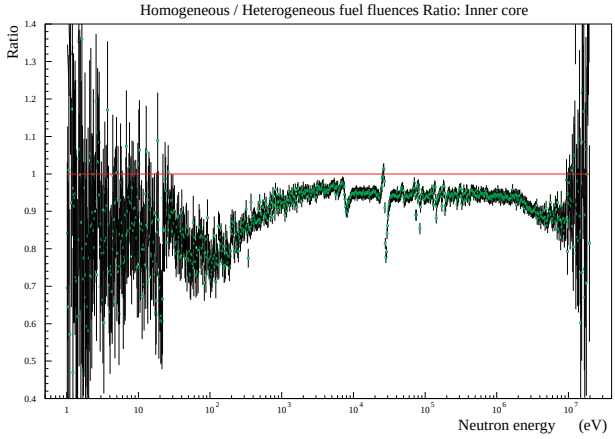

The fact that the ratio between the fluence and reaction rates between the two geometries are nearly independent of the neutron energy suggests that the difference is coming from the total neutron population. As the spallation source is expected to be nearly identical, the multiplication in the subcritical device should produce the observed difference.

The Keff has been computed for both geometries using the KCODE procedure of the MCNP code. In principle, the expected multiplication should be 1/(1-Keff), however as the fission source distribution produced by the spallation process is different from the eigen function of the transport equation, the net multiplication for a spallation source is slightly different. The values obtained from MCNP are shown in table C-2.

Table C-2:

	K_{eff}	Multiplication $1/(1-K_{eff})$	Net Multiplication (spallation source included)
Heterogeneous	0.9559±0.0009	22.7±0.5	25.6±0.3
Homogeneous	0.9505±0.0011	20.2±0.5	23.8±0.2

The resulting ratio homogeneous over heterogeneous in the net multiplication is 0.930 ± 0.014 which is in good agreement with the ratios obtained for the fluences and reaction rates, shown in tables C-3 and C-4.

Table C-3 **Average flux and energy produced by fission on each core zone for both LAHET/MCNP simulations**.

Flux (n/cm^2/proton)		**BR**	σ_{rel}	**OC**	σ_{rel}	**IC**	σ_{rel}
Heterogeneous	Fuel	3.58×10^{-3}	0.014	1.42×10^{-2}	0.014	3.25×10^{-2}	0.012
	Cladding	3.59×10^{-3}	0.014	1.42×10^{-2}	0.014	3.25×10^{-2}	0.012
	Lead	3.59×10^{-3}	0.014	1.42×10^{-2}	0.014	3.25×10^{-2}	0.012
Homogeneous		3.28×10^{-3}	0.010	1.31×10^{-2}	0.009	3.06×10^{-2}	0.008
Ratio (homogeneous/ heterogeneous fuel)		0.916	0.017	0.922	0.017	0.942	0.014
Fission energy produced (MeV/p)		**BR**	σ_{rel}	**OC**	σ_{rel}	**IC**	σ_{rel}
Heterogeneous		—	—	33719	0.014	21749	0.012
Homogeneous		—	—	31103	0.009	20414	0.008
Ratio (homogeneous/ heterogeneous fuel)		—	—	0.922	0.017	0.939	0.014

Table C-4 **Average capture rate of ^{232}Th and fission rate of ^{233}U on each core zone for both LAHET/MCNP simulations**

^{232}Th capture rate (capt/p)	**BR**	σ_{rel}	**OC**	σ_{rel}	**IC**	σ_{rel}
Heterogeneous	40.0	0.014	208.0	0.014	136.0	0.012
Homogeneous	37.0	0.009	193.3	0.009	129.0	0.008
Ratio (homog./ heterog.)	0.925	0.017	0.929	0.017	0.949	0.014
^{233}U fission rate (fiss/p)	**BR**	σ_{rel}	**OC**	σ_{rel}	**IC**	σ_{rel}
Heterogeneous	—	—	181.4	0.014	117.3	0.012
Homogeneous	—	—	167.4	0.009	110.2	0.008
Ratio (homog./ heterog.)	—	—	0.923	0.017	0.939	0.014

Conclusions of exercise C

Small but statistically significative differences on the fluences and in the main reaction rates are obtained, 5 to 9% depending on the core region, when comparing the homogeneous and heterogeneous models. Apart from few resonances of the cladding materials, the ratio of the results for the two geometrical descriptions is almost neutron energy independent.

This difference can be explained by a small difference on the effective multiplication factor, coming both from the small difference on the volume the fissile material is distributed over, and the different distribution of isotopes on the available volume.

However, in additional studies [8,9] it has been demonstrated that an homogeneous model with simple modifications can be adapted to provide acceptable description of the ADS behaviour on most usual studies.

D. Sensitivity studies on lead based ADS with UO_2 fuel

The present study shows the different estimations on Keff of an ADS-250, lead cooled, when using heterogeneous or homogeneous geometry description and different databases, for UO_2 fuels with different enrichments on ^{235}U. More details studies can be found at references [10,11,12]. The ADS geometry is always the same as in exercises A-C.

Different types of fuel have been considered in the neutronic simulation of ADS. In particular, for the first stages of a demonstration plant, it is presumably desirable a well-known fuel to be used. According to this, preliminary studies of the neutronic characteristics of a moderately enriched uranium dioxide ADS have been performed.

Several simulations had been performed both with fully detailed geometries (heterogeneous) and with simplified homogeneous geometries, using in each case first the JENDL-3.2 and second the ENDFB-VI.4 the nuclear data libraries. The results of the different simulations corresponding to different ^{235}U enrichments are shown on table D-1. These results, show a difference of up to 2 % between both libraries, owing to the differences in the lead elastic cross-section, ^{2}. The most important conclusion is that because the uncertainties associated to the method and cross section data libraries conservatives designs should be used. For example, a 18 % UO_2 enrichment gives a subcritical keff of 0.990 in a homogeneous simulation with JENDL3.2 data library, but it rises up to critical (1.012) in a heterogeneous simulation with ENDFB-VI R.4 data library.

Table D-1 **Keff vs. enrichment with different cross section data libraries and heterogeneous and homogeneous simulation**

% enrichment	**K_{eff} (JENDL3.2) homogeneous**	**K_{eff} (JENDL3.2) heterogeneous**	**K_{eff} ENDFBVI-R.4 homogeneous**	**K_{eff} ENDFBVI-R.4 heterogeneous**
10%	0.715±0.001	0.723±0.001	0.735±0.001	0.744±0.001
17%	0.961±0.02	0.967±0.001	0.982±0.001	0.985±0.001
18%	0.990±0.002	0.995±0.001	1.009±0.001	1.012±0.001

E. Sensitivity study on the spatial segmentation of lead based ADS geometry for burnup evolution simulation

Independently of the detail geometry of the ADS for the neutron transport calculation, a segmentation of the elements or groups of elements of the ADS core is required for burnup material evolution simulation.

The spatial dependence on the neutron flux intensity and its energy dependence inside the core, implies that a complete core fuel depletion calculation performed in zero-dimension approach could give inadequate results. Defining a core division in regions of almost constant reaction rates, several zero-dimension fuel burn up calculations can be performed. The ulterior addition of results will bring the time evolution of the full core taking into account the geometry dependencies [13,14]. The ideal

limit is an extremely fine core division, but this will mean a very large amount of depletion calculations. In our simulations we have divided the core in 10 different longitudinal zones. In total (120 fuel assemblies x 10) there are 1200 zones. Symmetric fuel assemblies are grouped for the material evolution simulations resulting only 140 independent cells.

In this paper we perform a study of the characteristics of the reaction rates of different isotopes in order to estimate the error from this spatial segmentation, and to achieve an equilibrium between computing time and simulation errors.

The calculated reaction rates can be separated into two factors: the so-called one group cross section (which means energy integrated, weighted by the proper flux spectrum) and the integrated flux. While the flux depends on the position and not on the studied reaction, the cross section in one group has nearly no dependence on the position.

The fuel assemblies in the core are divided in six groups of symmetric fuel assemblies, each of them are composed by 14 fuel assemblies. The figure E-1 shows the structure of the core identifying by labels, the groups of symmetric assemblies.

Figure E-1 **Structure of the core of the simulated ADS. The numbers identify groups of symmetric assemblies**

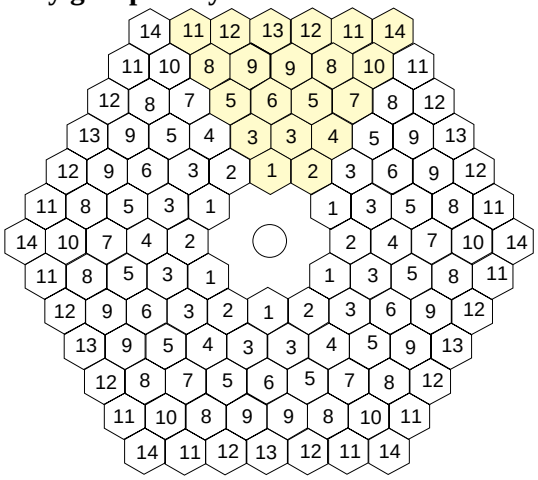

The comparison of the reaction rates of the most important isotopes on the different subcells (140 in total), allows to estimate their dependence with the position in the core, both along XY and Z. Figure E-2 shows the estimated maximum relative error in the concentration of ^{232}Th at any point within each subcells from the XY gradient of the evolution, after 1400 days of evolution at a total thermal power of 800 MW (average burnup of 120 GWd/HMT). This error is computed as half the maximum difference between the final concentration at one subcell and any of its neighbours. Figure E-3 presents the estimated maximum relative error in the ^{232}Th concentration due to the Z gradients, and Figure E-4 and E-5 the corresponding maximum relative errors for the ^{239}Pu concentrations.

Figure E-2. **Maximum relative error in the concentration of ^{232}Th, from the XY gradients of the reaction rates**

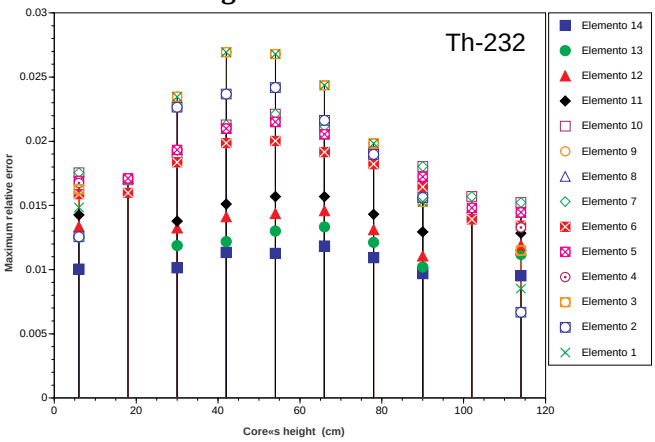

Figure E-3. **Maximum relative error in the concentration of ^{232}Th, from the Z gradients of the reaction rates**

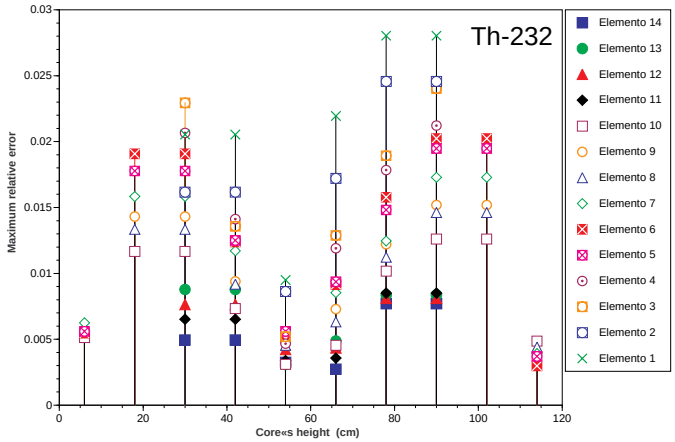

Figure E-4 **Maximum relative error in the concentration of ^{239}Pu, from the XY gradients of the reaction rates**

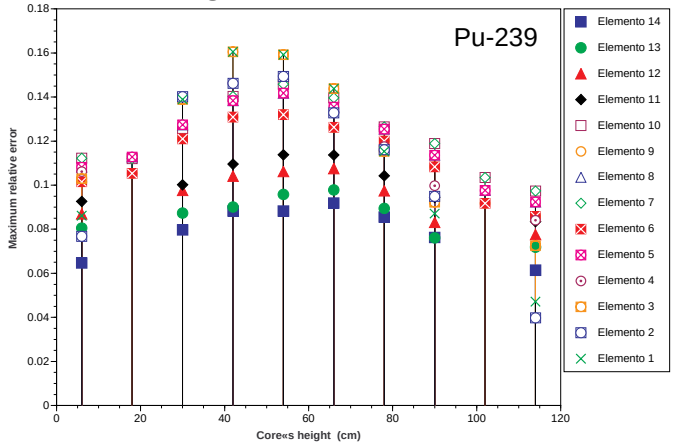

Figure E-5 **Maximum relative error in the concentration of ^{239}Pu, from the Z gradients of the reaction rates**

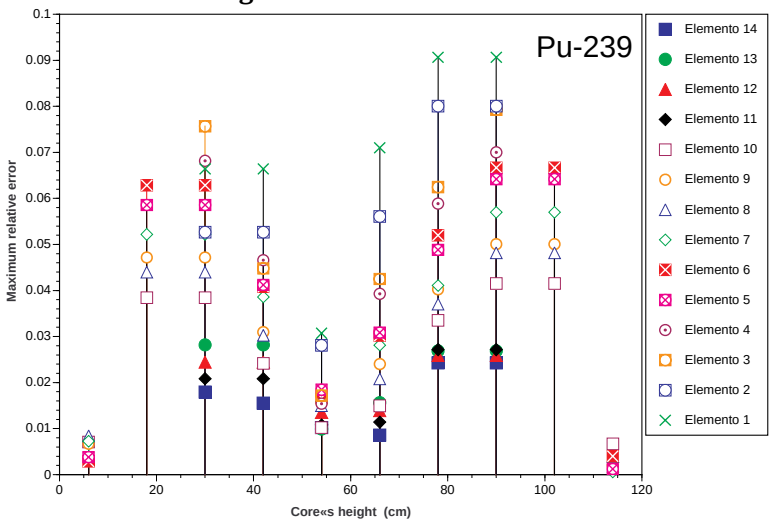

Figure E-6. **Reaction rate map per atom per second, close to the middle plane of the core**

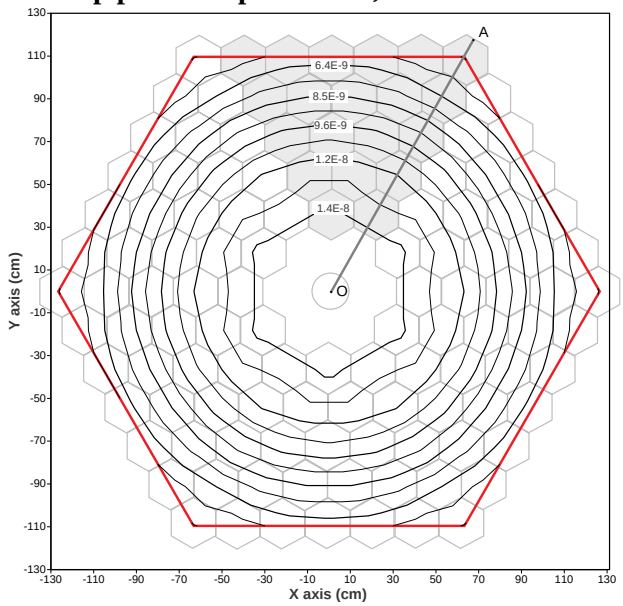

This error already moderated in magnitude have different signs for different positions within each subcell, and large compensations appear when computing the evolution of the material of the complete subcell or of the full system as a whole, reducing the final estimation error on the discharge isotopic composition. To estimate the error on the prediction for the material evolution of a subcell we have evaluated the map of reaction rates of fission and capture in ^{239}Pu, Figure E-6, and in particular the non linearity of these reaction rates along the O-A line of that figure. The results shown in Figure E-7, allow to estimate that the global error on the ^{239}Pu average concentration on the subcells is smaller than 0.4%.

Conclusions of exercise E

In order to prepare an isotopic-concentration time evolution calculation of an ADS, a core geometry segmentation must be done, dividing it into cells of almost constant reaction rates.

For a subcritical device such as our simulated ADS, the granularity in this division is mainly forced by the gradients of the flux in the core.

In our case dividing the core in 140 different zones (10 axial x 14 radial) we estimate an acceptable error (< 15%) in the reaction rates per atom along to the radial and axial directions, for individual fuel pins, and negligible errors for the average fuel subassembly composition evolution.

Figure E-7. **Radial distribution of the reaction rate per atom of Pu-239 along line O-A (Figure E-6)**

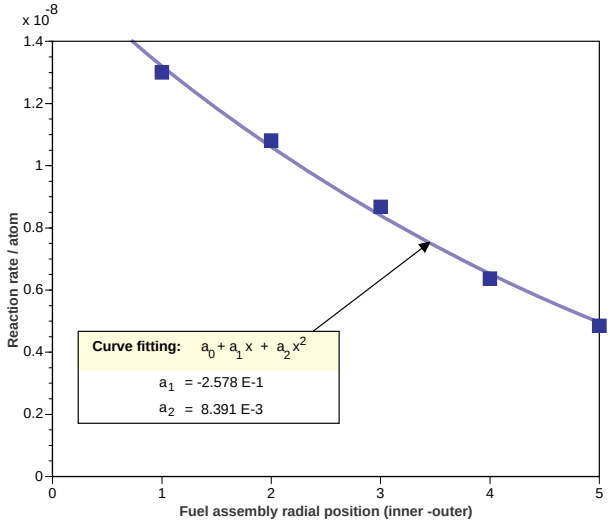

REFERENCES

[1] R.Fernández and E. González. Ejercicio de cálculo de la distribución de potencia específica de un diseño de Amplificador de Energía de 250 MW térmicos mediante LAHET/MCNP. CIEMAT/FACET/97-01.

[2] Embid, R. Fernández and E. González. Sensitivity study for the K_{eff} of a lead based ADS on the cross sections evaluations: ENDFB-6.4 and JENDL-3.2. CIEMAT REPORT 846 (1998).

[3] Briesmeister, Editor. MCNP™ - A General Monte Carlo N-Particle Transport Code. Version 4B. LA-12625 (1997).

[4] MacFarlane, D.W. Muir. The NJOY nuclear data processing system. Version 91. December 1994.

[5] EXFOR-97,Experimental Nuclear Reaction Data, IAEA.

[6] Prael and Henry Lichtenstein. User Guide to LCS: The LAHET Code System. LANL Group X-6 MS B226 (1989).

[7] Embid, R. Fernández, J.M. García-Sanz, and E. González. Estudio de la multiplicación neutrónica neta de un sistema ADS basado en plomo en función de la altura del haz de protones. Proceeding of the 24th Annual Meeting of the Spanish Nuclear Society at Valladolid, section 10-04 (1998).

[8] Fernández and E. González, Study on the Homogeneus and Heterogeneus Geometry Approaches for a Montecarlo Neutronic Calculation of the Energy Amplifier, CIEMAT REPORT 834 (1997).

[9] Embid, R. Fernández, J.M. García-Sanz, and E. González. Sensibilidad de la multiplicación neutrónica de un sistema ADS basado en plomo para su fuente de espalación en función de las librerías de secciones eficaces. Proceeding of the 24th Annual Meeting of the Spanish Nuclear Society at Valladolid, section 10-05 (1998).

[10] García-Sanz, M. Embid, R. Fernández and E.M. González. Estudio de K_{eff} para una geometría prototipo de ADS con combustibles de óxido de uranio. CIEMAT. DFN/TR-02/II-98 (1998).

[11] García-Sanz, M. Embid, R. Fernández y E. González. Cálculos neutrónicos para la definición de las primeras fases del laboratorio del amplificador de energía. CIEMAT. DFN/TR-04/II-98. (1998).

[12] García-Sanz, M. Embid, R. Fernández and E. González. Estudio de multiplicación neutrónica para un sistema subcrítico asistido por acelerador (ADS) con combustible de óxido de uranio y refrigerado por plomo. Proceeding of the 24th Annual Meeting of the Spanish Nuclear Society at Valladolid, section 10-11 (1998).

[13] Fernández, M. Embid, J.M. García-Sanz and E. González. Diseño de un procedimiento de simulación combinada de la evolución isotópica y neutrónica en un sistema subcrítico asistido por acelerador. Proceeding of the 24th Annual Meeting of the Spanish Nuclear Society at Valladolid, section 10-10 (1998).

[14] Fernández, M. Embid, J.M. García-Sanz and E. González. Performance on actinide transmutation of lead-thorium based ADS. Presented to this conference.

MCB: A CONTINUOUS ENERGY MONTE CARLO BURNUP SIMULATION CODE

Jerzy Cetnar, Jan Wallenius and Waclaw Gudowski
Department of Nuclear and Reactor Physics
Royal Institute of Technology
100 44 Stockholm,
Sweden

Abstract

A code for integrated simulation of neutronics and burnup based upon continuous energy Monte Carlo techniques and transmutation trajectory analysis has been developed. Being especially well suited for studies of nuclear waste transmutation systems, the code is an extension of the well validated MCNP transport program of Los Alamos National Laboratory. Among the advantages of the code (named MCB) is a fully integrated data treatment combined with a time-stepping routine that automatically corrects for burnup dependent changes in reaction rates, neutron multiplication, material composition and self-shielding. Fission product yields are treated as continuous functions of incident neutron energy, using a non-equilibrium thermodynamical model of the fission process. In the present paper a brief description of the code and applied methods are given.

Introduction

Currently, the Monte Carlo transport code MCNP developed at Los Alamos National Laboratory is regarded as state of the art in the reactor neutron transport field [1]. Other codes are either benchmarked against MCNP (e.g. CASMO and ERANOS), or are not validated in the same respect as MCNP is (e.g. CERN's EET Monte Carlo code). Since MCNP itself does not calculate nuclide density evolutions, simulations of burnup in a material subject to intense neutron irradiation has until now been made by using simplified integrated transport and burnup codes like BISON, or by linkage of advanced neutronics codes as MCNP and ERANOS with specialised burnup codes like CINDER90, ORIGEN2 and DARWIN. The exception is the general particle transport and burnup Monte Carlo code developed by the EET-group at CERN, which however has not yet been made available for independent evaluation.

Such coupling of codes leaves the field open for inconsistencies on form of basic data discrepancies. It further sets high demands on the user capability of assigning time stepping grids adequate for spectrum changes and self shielding effects to be correctly modelled. Especially in the field of nuclear waste transmutation, where correct prediction of minor actinide and fission product density evolution of are of much higher significance than in simulations of commercial nuclear power plants, there is a need for better modelling tools. Hence it was undertaken by the present authors to extend the most advanced and best validated code for neutron transport available - MCNP - with advanced nuclide density evolution capabilities, including transmutation trajectory analysis, in order to create a fully integrated, well validated Monte Carlo Burnup simulation code - MCB.

Requirements

The requirements of the code development are set by the demand of a correct modelling of critical and sub-critical waste transmutation systems. These are supposed to transmute extraordinary large fractions of original materials present in the system. For instance, resulting material compositions after 20% heavy atom burnup and up to 50% long lived fission product transmutation during a single irradiation cycle must be correctly predicted by the code, which means that significant spectrum changes and self shielding effects have to be accommodated for. Further, in order to optimise fuel and waste management, it is advantageous to apply the transmutation trajectory analysis method, which provides additional information of the transmutation process, as compared to the exponential matrix method.

Implementation

Physical Data

The basic cross section and decay data used by MCB consist of:

- Decay data including decay constants and branching ratios for over 2400 nuclides. The decay data file was prepared on the basis of the Table of Isotopes (ToI) version 8E.
- Neutron transport cross section libraries for about 300 nuclides, prepared with NJOY at various temperatures on the basis of the room temperature evaluations ENDF/B-VI, JEF2.2 and JENDL3.2.

- Neutron reaction cross section libraries for about 400 additional nuclides (for which transport cross section evaluations do not exist), prepared with NJOY at various temperatures on the basis of the EAF evaluation.
- Continuous energy fission product yield libraries for 36 actinides, including yields of over 1000 fission products. The library was constructed using an updated version of the THERMO code, which calculates independent yields using a non-equilibrium thermodynamical model [2]. See below for details.
- Data for effective dose per unit intake for 738 nuclides, prepared on the basis of the Basic Safety Standards of IAEA.
- Meta-stable to ground state capture ratios for neutron capture on ^{241}Am and ^{243}Am according to the evaluation of Mann and Schenter [3].

All unique (with respect to nuclide) transport and reaction cross sections given in the XSDIR file are loaded during initialisation of MCB. Presently, it is the first occurrence of a nuclide that is loaded, if paths to different evaluations are given. During calculation, only cross sections for nuclides that have concentrations larger than a given threshold will be used. This threshold may be changed in the input file, which might have large influence on the time used by MCB for particle transport.

Material specifications

Material specifications are simplified with respect to the MCNP input format. In MCB, chemical symbols may be used instead of charge numbers, e.g. Pu239.60c replaces 94239.60c, and Pb replaces 82000.xxc. The evaluation index in the latter case is fixed by the first occuring library path in the XSDIR file. Specifying the index explicitly overrides the XSDIR file ordering.

In addition to standard MCNP material specifications “burnup”, “residual” and “mixed” materials are introduced in MCB. Burnup materials are not used in transport calculations unless their macroscopic cross section contribute to the total cross section with a fraction larger than a discrimination level supplied in the input file. Residual material have no defined density, and are used only for transmutation transition calculations. Finally materials may be mixed using the mixed material specification, which greatly simplifies initial system definitions.

Burnup run specifications

Materials for which burnup is to be calculated (not necessarily all materials) are specified with the “BURN” command. If several of the cells in the system geometry have the same material number, they will constitute a burnup zone, where nuclide evolution will be calculated from averaged transmutation rates. This can be used in symmetrical systems to diminish statistical fluctuations.

The physical conditions of the irradiation (and decay) simulation are fixed by specifying time periods of constant conditions, and corresponding source strength or heat dissipation (power). If neither power nor source strength is specified, or both are set to zero, plain decay of unstable nuclides takes place.

The constraints of the automated time-stepping routine are prescribed in the input file by specifying longest allowed time step (equal to the first trial time step), allowed variation of k-eigenvalue, neutron multiplication and/or reaction rate during a time step. Discrimination levels of macroscopic cross section contributions and nuclide to nuclide transmutation transitions may also be specified, as well as a half-life threshold for treatment of fast decaying nuclides. All these variables have default values, and hence are not required input data.

Flow sheet of code run

At start-up of the code, all unique cross section files pointed to in the XSDIR file are loaded, as described previously. The program checks if nuclides with short half-life exist in the materials specified, and force them to decay before making a calculation of the k-eigenvalue of the system. If this is lower than a given threshold, a source particle transport run is made where system power and transmutation rates are calculated "in flight". Otherwise, the particle flux is assumed to be sufficiently well described by the eigenflux and a new KCODE run is made, including sampling of heating and transmutation rates. Then, transmutation trajectories are selected, and the nuclide density evolution is calculated during the whole trial time step. The macroscopic cross sections of the appearing nuclides are calculated in order to check that they do not exceed the fraction of the total cross section set by the discrimination level. Similarly, a k-eigenvalue calculation is made to assure that changes in asymptotic neutron multiplication stays within the prescribed range. If either of these conditions are not fulfilled, a smaller time step is set for a renewed nuclide density prediction. Finally, new nuclide concentrations in the burnable materials are initialised and a new particle transport run is initiated.

Fission Product Yield Model

Since experimental data on fission product yields of the minor actinides are scarce, and the energy dependence of mass and charge distributions are only known for three points (at best), there was a need for a robust theoretical model to create energy dependent fission product yield libraries. In MCB, the non-equilibrium thermodynamical model of Grashin is used for this purpose [2]. The model is based on a new theoretical understanding of quantum mechanical processes in systems having too many free variables for non-statistical methods to be useful, while being too short-lived for standard equilibrium thermodynamics to be fully applicable. By introducing the concept of "free energy" of the excited compound nucleus, the model calculates the probability of finding final states of two (or three) fission products with concomitant release of a given number of neutrons within the manifold of the initial state. Thus the energy dependence of the fission product yield enters as a fundamental property in the model. Shell effects are taken into account , and most free parameters are fixed by fitting model predictions with experimental yields for a fission of a single nuclide at a single energy. For other nuclides only one free parameter, the ground state temperature, remains. This can be determined from e.g. the ratio of peak to fission valley yields, which is better known for the minor actinides than individual yields. Since yield distributions for thermal fission of ^{235}U are comparatively well known, errors in the low yield predictions for arbitrary actinides should generally not be worse than the same errors for ^{235}U. This is of great significance in transmutation simulations, as many system proposals are based on pure minor actinide fuels, which existing commercial codes never were intended to model accurately.

Figure 1 shows the predicted fission product mass yields at thermal incident neutron energies for ^{241}Pu and ^{245}Cm (left), and the energy dependence of the mass yield for ^{241}Pu (right).

Figure 1. **Fission product mass yields in thermal neutron induced fission of ^{241}Pu and ^{245}Cm (left). Incident neutron energy dependence of the mass yield in fission of ^{241}Pu (right). Note the differences in yield of the light peak and the fission valley, respectively.**

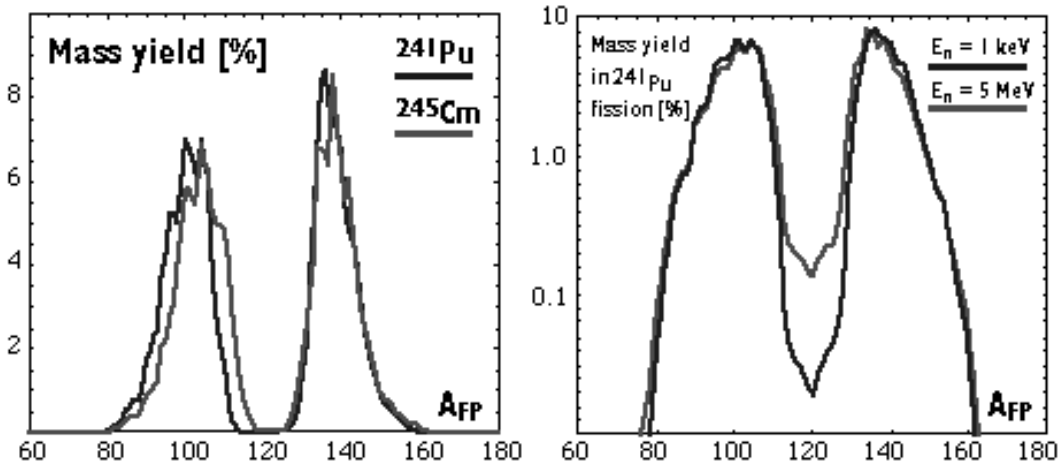

Note that the cumulative yield of ^{90}Sr varies considerably with mass of the fissioning actinide, being about 6% for ^{235}U, but less than 1% for ^{245}Cm. The increase of yield in the fission valley with neutron energy leads to an increased production of e.g. the raditoxic long lived nuclide ^{126}Sn by a factor of two when raising the incident neutron energy from 1 keV up to 1 MeV. The importance of including correct fission product yields in calculations of radiotoxic inventories thus seems very clear.

Discussion

The accurate modelling of high burnup waste transmutation systems demands a well validated integrated particle transport and burnup code. MCB, here presented, may fulfil this purpose. The main parts of the code being implemented and under testing, minor improvements still needs to be done before public release. The authors are well aware of the benefits of a large group of code evaluators, hence the release is expected to take place before the end of June 1999. Future versions of the code will include integration with MCNPX for high energy proton and neutron transport, as well as tallying of atomic recoil spectra for radiation damage estimations.

REFERENCES

[1] MCNP - A general Monte Carlo N-Particle transport code, version 4B, LA-12625-M. Editor, J.F. Briesmeister, Los Alamos National Laboratory (1998).

[2] A. Grashin, A. Jefimenko and V. Kolobashkin, Izvestiya Akademii Nauk SSSR 49 (1985) 188 (in russian).

[3] F.M. Mann and R. E. Schenter, Nuclear Science and Engineering 63 (1977) 242.